A Constitutive Heterochromatic Region Shapes Genome Organization and Impacts Gene Expression in *Neurospora crassa*

Andrew T. Reckard[1], Abhishek Pandeya[2]*, Jacob M. Voris[1]*, Carlos G. Gonzalez Cruz[1], Oluwatosin Oluwadare[2], and Andrew D. Klocko[1‡]

[1]Department of Chemistry & Biochemistry, University of Colorado Colorado Springs, Colorado Springs, CO 80918, USA

[2]Department of Computer Science, University of Colorado Colorado Springs, Colorado Springs, CO 80918, USA

*Equal Contribution

‡Corresponding Author: Andrew D. Klocko, email: aklocko@uccs.edu

Abstract

Background: Organization of the eukaryotic genome is essential for proper function, including gene expression. In metazoans, chromatin loops and Topologically Associated Domains (TADs) organize genes into transcription factories, while chromosomes occupy nuclear territories in which silent heterochromatin is compartmentalized at the nuclear periphery and active euchromatin localizes to the nucleus center. A similar hierarchical organization occurs in the fungus *Neurospora crassa* where its seven chromosomes form a Rabl conformation typified by heterochromatic centromeres and telomeres independently clustering at the nuclear membrane, while interspersed heterochromatic loci aggregate across Megabases of linear genomic distance to loop chromatin in TAD-like structures. However, the role of individual heterochromatic loci in normal genome organization and function is unknown.

Results: We examined the genome organization of a Neurospora strain harboring a ~47.4 kilobase deletion within a temporarily silent, facultative heterochromatic region, as well as the genome organization of a strain deleted of a 110.6 kilobase permanently silent constitutive heterochromatic region. While the facultative heterochromatin deletion minimally effects local chromatin structure or telomere clustering, the constitutive heterochromatin deletion alters local chromatin structure, the predicted three-dimensional chromosome conformation, and the expression of some genes, which are qualitatively repositioned into the nucleus center, while increasing Hi-C variability.

Conclusions: Our work elucidates how an individual constitutive heterochromatic region impacts genome organization and function. Specifically, one silent region indirectly assists in the hierarchical folding of the entire Neurospora genome by aggregating into the "typical" heterochromatin bundle normally observed in wild type nuclei, which may promote normal gene expression by positioning euchromatin in the nucleus center.

43 **Keywords:** genome organization, chromosome conformation, heterochromatin, *Neurospora crassa*,

44 gene expression

Introduction

Correct genome organization, including proper chromosome folding, is necessary for DNA-templated processes to function normally, including for wild type (WT) control of gene expression [1–5]. Indeed, improper DNA folding altering transcriptional patterns occurs in human cancer cells [6–8]. Eukaryotic genomes hierarchically fold, as DNA molecules wrap around histone octamers to form chromatin fibers, which are extruded into globules ("loops") by cohesin, and multiple loops compact into Topologically Associated Domains (TADs) [9–17]. TADs of similar transcriptional activity compartmentalize in the nucleus [10, 11, 17]. Specifically, the more open, gene-rich, and actively transcribed euchromatin primarily localizes to the nucleus center, while the silent, gene-poor, and compact heterochromatin is confined to the nuclear periphery [18–20]. Heterochromatin segregation may drive chromatin compartmentalization, although transcriptional activity might force silent genomic loci to the nuclear periphery [19, 21]. In metazoans, the formation of individual chromosome territories – typified by extensive intra-chromosomal contacts – leads to the clustering of heterochromatic regions within chromosomes [22, 23]. In contrast, the independent aggregation of the heterochromatic centromeres and telomeres of fungal chromosomes into a Rabl conformation promotes widespread intra- and inter-chromosomal heterochromatic contacts [9, 24–26]. All told, heterochromatin bundling is a conserved feature of eukaryote genome organization.

Fungi are excellent genome organization models. Fungal genomes are partitioned into euchromatin and heterochromatin, resembling the genomes of metazoans, and the heterochromatin of many filamentous fungi, including *Neurospora crassa*, is subdivided into permanently silent constitutive heterochromatin and temporarily silent facultative heterochromatin [27–29]. The adenine and thymine (AT)-rich, gene-poor, and repetitive constitutive heterochromatic regions, comprising ~16% of the Neurospora genome, are marked by the tri-methylation of lysine 9 on histone H3 (H3K9me3); this mark is catalyzed by the histone methyltransferase DIM-5 (KMT1) [28,

69 30–32]. Specific H3K9me3-marked regions found within the seven Neurospora chromosomes
70 ("Linkage Groups" [LGs]) include the regional centromeres, the 14 telomeres, and ~200
71 interspersed heterochromatic regions [28, 32]. In contrast, Neurospora facultative heterochromatin
72 is delineated by the subtelomeric di- or tri-methylation of lysine 27 on histone H3 (H3K27me2/3)
73 catalyzed by the SET-7 (KMT6) histone methyltransferase subunit of the Polycomb Repressive
74 Complex 2 (PRC2) [33–35]. In the Neurospora three-dimensional (3D) genome organization, as
75 assessed by in-nucleus chromosome conformation capture with high-throughput sequencing (*in*
76 *situ* Hi-C), robust intra- and inter-chromosomal heterochromatic contacts occur across Megabases
77 of linear genomic distance, yet heterochromatin minimally interacts with euchromatin, highlighting
78 the compartmentalization of fungal chromatin [9, 24, 25]. Several Ascomycete fungi cluster
79 heterochromatic regions at the base of TAD-like structures, suggesting heterochromatin aggregation
80 may be a conserved mechanism organizing fungal genomes [9, 24–26, 36]. Further, subtelomeric
81 facultative heterochromatin helps chromosome ends associate with the Neurospora nuclear
82 periphery [37]. Together, both heterochromatin types organize the Neurospora genome in a Rabl
83 chromosome conformation.

84 To understand the importance of individual facultative and constitutive heterochromatic regions
85 in Neurospora 3D genome organization, we performed chromatin-specific *in situ* Hi-C on a strain
86 deleted of ~47.4 kilobases (kb) within a H3K27me2/3 domain on the LG VI left arm [34], as well as
87 a strain deleted of an ~110 kb H3K9me3 domain on the LG II right arm ("ΔLGIIK9het25"). While the
88 H3K27me2/3 deletion minimally impacts genome organization, the ΔLGIIK9het25 allele alters the
89 inter-heterochromatic region aggregation, which may increase 3D genome organization variability,
90 and changes the chromatin structure at the deletion site, while nearby AT-rich loci still retain
91 substantial H3K9me3 enrichment. Individual chromosomes in a ΔLGIIK9het25 strain are predicted
92 to have qualitatively different 3D structures than those in a WT strain, and numerous genes are

93 upregulated with the LGIIK9het25 deletion, possibly due to altered gene positioning within the 3D
94 genome. We conclude that a single constitutive heterochromatic region helps form the "typical"
95 genome organization and promotes normal genome function in WT Neurospora.
96

97 **Materials and Methods**

98 *Strains and growth conditions*

99 *Neurospora crassa* strains WT N150 (derived from the strain 74-OR23-IVA [Fungal Genetics
100 Stock Center #2489]), N2930 (*mat A his-3;* Δ*mus52::bar*$^{+}$), N3944 (mat x; Δ*dim-5::bar*$^{+}$), and N4933
101 (*mat a*; Δ47.4 kb::*hph*$^{+}$) were gifts from Eric U. Selker (University of Oregon). All strains were grown
102 with 1x Vogels minimal medium + 1.5% sucrose and supplements at 32°C [38].

103 The ΔLGIIK9het25 (NKL2) strain, which replaces 110,609 basepairs (bp) of AT-rich DNA in
104 H3K9me3-enriched region number 25 on LG II (between bp 3,602,033 and 3,712,857 of Neurospora
105 reference genome version 14 [nc14]) [24] with 1,401 bp of the P_{trpC}*::hph* hygromycin resistance
106 cassette (a net genome deletion of 109,208 bp), was created by split marker gene replacement.
107 Briefly, the ~1,000 bp upstream of LGIIK9het25 was PCR amplified with oligonucleotides ("oligos")
108 oKL14 and oKL15, while the ~1,000 bp downstream of LGIIK9het25 was amplified with oligos
109 oKL18 and oKL19, by Phusion DNA polymerase (cat# F530-L; ThermoFisher Scientific) using the
110 manufacturer's conditions; oligos oKL15 and oKL18 had ten 5' complementary nucleotides specific
111 to the P_{trpC} promoter and *hph* gene 3' end, respectively. Oligo sequences are provided in Table S1.
112 DNA fragments were gel purified using the GenCatch Gel Extraction Kit (cat# 2260250; Epoch Life
113 Sciences), and split marker fragments fusing the LGIIK9het25 upstream to the P_{trpC} promoter ("UP";
114 oKL14 and 2955) or fusing the *hph* gene to the LGIIK9het25 downstream ("DOWN"; oligos 2954 and
115 oKL19) were PCR amplified with the upstream and downstream fragments and a plasmid encoding
116 the *hph* gene (p3xFLAG::hph::LoxP) [39] using LA Taq (cat# RR002M; Takara), and gel purified. The

117 UP and DOWN split marker fragments were transformed into N2930 by electroporation (BioRad
118 MicroPulser Electroporator, cat# 1652100EDU). Hygromycin resistant colonies were selected on 1x
119 Vogels+FGS media with 100 μg/mL hygromycin (cat# ant-hg-5; Invivogen). Genomic DNA was
120 isolated from resultant colonies using standard protocols [40], and tests of proper hygromycin
121 cassette integration at the LGIIK9het25 locus was performed by PCR using oKL49 and 2955 for the
122 left border, 2954 and oKL50 for the right border, and oKL49 and oKL50 for the entire integrated
123 P_{trpC}*::hph* gene. Positive integrant strain tKL1A-2 was crossed to N150 (xKL9AR) and genomic DNA
124 was isolated from hygromycin resistant progeny; similar PCR reactions were performed to confirm
125 the presence of the ΔLGIIK9het25 allele in individual cross progeny. PCR with oligos oKL55 and
126 oKL56 determined Δ*mus-52::bar* allele absence, and the strain mating type was established by
127 crosses with known mating type strains. The final homokaryotic strain, NKL2, from cross progeny
128 xKL9AR-17 contains only the ΔLGIIK9het25 deletion (NKL2 genotype: *mat A;* Δ*LGIIK9het25::hph*).
129
130 *Hi-C library construction and bioinformatic analyses*
131 *In situ* Hi-C was performed as described [24, 25]. Hi-C libraries were Illumina sequenced at the
132 Genomics and Cell Characterization Core Facility (GC3F; University of Oregon), either on a Hi-Seq
133 2500 as PE100 reads or a NovaSeq 6000 as PE59 reads. For comparison to mutant Hi-C datasets,
134 WT *Dpn*II and *Mse*I *in situ* Hi-C datasets (NCBI Gene Expresssion Omnibus (GEO) accession number
135 GSE173593) [24] were generated by extracting the number of total reads from WT datasets using
136 the sed command for similar numbers of valid reads as mutant datasets. Merged fastq file reads, or
137 individual replicate reads, were mapped with bowtie2 [41] to nc14 [24], or the nc14-derived
138 reference "NKL2 genome" where the LGIIK9het25 sequence is replaced with the P_{trpC}*::hph* sequence.
139 Output sam files were used to build the initial contact probability matrix at a high [1 kb] resolution
140 with hicExplorer software package [42]. Merged contact probability matrices were used to generate

141 lower resolution contact matrices (hicMergeMatrixBins), compare WT and mutant datasets
142 (hicCompareMatrices), KR correct matrices (hicCorrectMatrix), assess TADs (hicFindTADs [using --
143 correctForMultipleTesting fdr [false discovery rate], --thresholdComparisons 0.3, and --delta 0.15
144 values for TAD bed files] and hicPlotTADs), and generate images (hicPlotMatrix); replicate similarity
145 was analyzed with (hicCorrelate); additional TAD prediction was performed with Topdom [43].
146 Chromosome 3D structure prediction was performed with 3DMax (https://github.com/BDM-
147 Lab/3DMax) [44] while Neurospora 3D genome structure prediction was performed by LorDG [45],
148 using custom scripts tailored to fungal chromosome biology; scripts are available on the Oluwadare
149 lab GitHub (https://github.com/OluwadareLab/Fungi_3DGenome). Structure prediction contact
150 matrices were made by merging *Dpn*II and *Mse*I matrices (hicSumMatrices) and converting the .h5
151 output to NxN text files with a custom script [24] (https://github.com/Klocko-Lab). Output PDB
152 files were displayed on ChimeraX [46] with bins containing differentially expressed genes or
153 chromosomal features manually colored, and high-resolution images were used to create figures.
154 PDB files for all 3D structures are available on Zenodo (10.5281/zenodo.11245552).
155
156 *ChIP-seq library construction and bioinformatic analyses*
157 Chromatin Immunoprecipitation-sequencing (ChIP-seq) was performed as described [47], using
158 anti-H3K9me3 (Active Motif; cat# 39161, lot# 30220003) and anti-H3K27me2/3 (Active Motif; cat#
159 39535, lot# 23120014) antibodies. All ChIP-seq libraries were Illumina sequenced at the GC3F on a
160 NovaSeq 6000 as SR118 reads. Fastq dataset files were mapped to nc14 or the NKL2 genome with
161 bowtie2 [41], converted to bam files, sorted, and indexed with samtools [48], made into bigwig files
162 with Deeptools [49], and displayed on Integrative Genomics Viewer (IGV) [50], with saved png
163 images used for figure creation. Previously published NCBI GEO or the NCBI Sequence Read Archive
164 (SRA) datasets for WT H3K9me3 (GEO accession numbers GSE68897 and GSE98911), WT

165 H3K27me2/3 (GEO accession numbers GSE68897 and GSE100770), Δ*dim-5* H3K27me2/3 (GEO
166 accession number GSE68897 and SRA accession number SRP058573), and input Neurospora DNA
167 (GEO accession number GSE150758) [32, 51–54], were mapped to the nc14 genome [24] and used
168 to create bigwig files, as above, for image generation.
169
170 *Total RNA isolation, polyadenylated RNA-seq library construction, and bioinformatic analyses*
171 Total RNA was isolated from overnight liquid cultures of Neurospora strains grown in 1x Vogels,
172 1.5% sucrose plus supplements [33, 37]. Cultures were harvested by vacuum filtration, placed in
173 2.0mL screw-top tubes, and 300µL of acid washed glass beads suspended in dH_2O (150-212µm,
174 Sigma Aldrich cat# G1145-10G), 350µL Acid Phenol:chloroform (5:1; ThermoFisher cat# AM9720),
175 and 350µL NETS (300mM NaCl, 1mM EDTA, 10mM Tris pH 7.5, 0.2% SDS) were added. Samples
176 were vortexed for 10 minutes at maximum speed and centrifuged at 4°C for 5 minutes at 13k rpm.
177 The aqueous layer was transferred to two tubes (~250µL each), 650µL of cold 100% EtOH was
178 added, and RNA was precipitated on ice for 10 minutes and pelleted by microcentrifugation at 4°C
179 for 10 minutes at 13k rpm. The pellet was washed with cold 70% EtOH (made with DECP-treated
180 dH_2O), the supernatant was removed, and pellets were allowed to air dry for 15 minutes and
181 resuspended in 50µL DEPC-treated dH_2O. Insoluble material was removed by centrifugation, and
182 the initial RNA concentration was measured by Nanodrop. Total RNA (10µg) was resuspended in
183 50µL of DEPC-treated dH_2O, and the Zymo RNA Clean and Concentrator kit (Zymo Research cat#
184 R1013) was used for RNA cleanup per the manufacturer's protocol; the 15µL elution was divided
185 into 4µL for Qubit concentration (RNA HS assay kit; ThermoFisher Scientific, cat# Q32852) and
186 TapeStation (Agilent) quality control analysis, while the remaining 11µL was stored at -80oC. Only
187 total RNA samples with high ribosomal RNA to messenger RNA (mRNA) ratios were used for library
188 construction. Polyadenylated mRNA (polyA mRNA) was selected with the NEBNext Poly(A) mRNA

189 Magnetic Isolation Module (New England Biolabs [NEB], cat# E7490L) and polyA mRNA sequencing
190 libraries were generated with the NEBNext Ultra II Directional RNA Library Prep Kit for Illumina
191 (NEB, cat# E7760L and E7765L) per the manufacturer's protocols; quadruplicate polyA mRNA-seq
192 replicate libraries were constructed for each strain. All polyA mRNA-seq libraries were Illumina
193 sequenced at the GC3F on a NovaSeq 6000 as SR118 reads. Raw fastq files were mapped to the nc14
194 genome using HiSat2 [55], and htseq-count [56] generated gene count files. Differential Expression
195 analysis between strains was performed with DESeq2 [57] in R/Rstudio [58, 59], selecting
196 significantly changed genes as those with expression $\log_2 > 3.0$ or $\log_2 < -3.0$ and an adjusted p-value
197 < 0.001; bed files for display on IGV were generated from the DESeq2 output gene lists in Microsoft
198 Excel, and volcano plots of $\log_2$ fold change vs. adjusted p-value were generated in R/R studio.
199

200 **Results**

201 ***Loss of a H3K27me2/3-enriched region minimally affects the local chromatin landscape.***

202 Since interactions between regions of similar heterochromatin type comprise many of the
203 strongest intra-chromosomal contacts in the Neurospora genome [24, 25], we examined how
204 deletions of either type, facultative or constitutive heterochromatin, could impact fungal
205 heterochromatin clustering. Starting with facultative heterochromatin, we examined a previously
206 constructed strain, N4933, originally used to assess position-dependent signals for H3K27me2/3
207 deposition in the Neurospora genome [34]. N4933 harbors a 47.4 kb deletion, from basepairs
208 175,121 to 222,557 on LG VIL, which removes fourteen H3K27me2/3-enriched genes within a
209 larger facultative heterochromatin domain (this strain is named "ΔK27" for brevity). To assess how
210 ΔK27 impacts genome organization, we performed two *in situ* Hi-C replicates with *Dpn*II to capture
211 chromatin interactions within gene-rich DNA of a higher guanine and cytosine percentage, including
212 in facultative heterochromatic regions. Our replicates show highly similar Hi-C contact matrices

213 across LG VI and are highly correlated (Figure S1), allowing replicate merging into a single Hi-C
214 dataset with 9.2 million (M) valid reads. For comparison, we processed an identical number of valid
215 Hi-C reads from our WT *in situ Dpn*II Hi-C dataset [24]. Our initial observation is that, despite having
216 similar valid read numbers, the ΔK27 dataset is slightly biased in capturing more local contacts and
217 less heterochromatin interactions, likely due to variability in ΔK27 Hi-C experiments, with reduced
218 AT-rich heterochromatin ligation since the underlying DNA has less *Dpn*II sites. Indeed, decreased
219 inter-centromeric contacts in the ΔK27 dataset, relative to the WT dataset, occur in raw contact
220 matrices (Figures 1, S2-S3). Inter-centromeric interactions are present upon Knight-Ruiz (KR) [60]
221 correction (Figure S2-S3), indicating capture of biologically relevant structures. However, the
222 decrease in moderate and long-range contacts in the ΔK27 dataset is evident when this contact
223 matrix is directly compared to the WT dataset (Figure S3). Therefore, we focused on the local
224 chromatin changes on LG VI that manifest with the ΔK27 deletion.

225 On WT LG VI, we observe consistent off-diagonal contacts that decrease with genomic distance,
226 in addition to strong inter-telomeric contacts and the insulation of centromeric DNA from local
227 euchromatin, in both raw and KR corrected heatmaps (Figure 1A). A higher resolution (5kb) WT
228 heatmap of the 500 kb surrounding the region targeted for deletion in N4933 shows a similar
229 inverse relationship between contact strength and genomic distance (Figure 1A). In contrast, the
230 ΔK27 deletion Hi-C, mapped to the Neurospora reference genome version 14 (nc14) [24], appears
231 as a white cross emanating from the deletion locus indicating a gap in mappable Hi-C reads (Figure
232 1B), since this DNA was not present during Hi-C ligation capture. This gap occurs in both the raw
233 and KR corrected contact probability heatmaps, although the diagonal base in the KR corrected
234 heatmap presents with signal (Figures 1B-C), due to miniscule contact probabilities assigned to bins
235 covering repeated DNA sequences prior to matrix correction (Figure S4); KR correction enhances
236 this bias. Importantly, stronger off diagonal signal at the boundary intersections of the facultative

237 heterochromatin deletion appear (Figures 1B-C, black arrowheads), showing how new interactions
238 occur between the H3K27me2/3-enriched chromatin flanking the ΔK27 deletion. Interestingly, the
239 *sly1-1* transposase gene NCU09969 (Figure 1C, gray arrowhead) is devoid of Hi-C signal in N4933,
240 suggesting the ΔK27 strain had a transposition event. Regarding telomere clustering, the ΔK27
241 strain still forms intra- and inter-chromosomal subtelomeric contacts (Figures 1D-E), with strong
242 interactions between the terminal ~100kb of H3K27me2/3-enriched chromatin at chromosome
243 ends. We conclude a deletion of a H3K27me2/3-enriched region minimally impacts the organization
244 of the remaining facultative heterochromatic regions on LGVIL.
245
246 ***Deletion of a ~110 kb constitutive heterochromatic region alters silent region clustering.***
247 In Neurospora nuclei, gene-poor AT-rich constitutive heterochromatin is compartmentalized
248 from gene-rich euchromatin and most facultative heterochromatin [24, 47]. To ask if an individual
249 constitutive heterochromatic region impacts Neurospora genome organization and function, we
250 deleted a 110,609 bp H3K9me3-enriched region on LG IIR, aptly called "LGIIK9het25" as this region
251 is the 25th constitutive heterochromatic region from the LG II left telomere. We chose to delete this
252 second largest AT-rich region on LG II, since there would be a high probability of observing genome
253 organization changes without compromising chromosome function if the centromere was removed.
254 Using split-marker homologous recombination in a Δ*mus-52* strain [61], we replaced the 110.6 kb
255 LGIIK9het25 with a hygromycin resistance gene (hygromycin phosphotransferase; *hph*) controlled
256 by a strong constitutive *trpC* promoter (a P_{trpC}*::hph* cassette; Figure S5A). We note a similar-sized
257 DNA replacement could have more accurately represented the LG II chromosome length, but we
258 wanted to avoid cryptic promoters, repetitive sequences for RIP [28, 62, 63], or AT-rich DNA
259 sequences forming novel constitutive heterochromatic regions within the inserted DNA; progressive
260 LGIIK9het25 region deletions might have elucidated additional changes to heterochromatic loci

261 bundling patterns. We also attempted other heterochromatic region deletions using the
262 nourseothricin acetyltransferase (*nat1*) resistance gene [64], but did not get primary transformants,
263 possibly due to immediate silencing of the AT-rich *nat1* gene at the targeted constitutive
264 heterochromatic loci. We successfully obtained hygromycin-resistant primary transformants
265 deleted of LGIIK9het25 (ΔLGIIK9het25), in which 109,208 bp are removed from the Neurospora
266 genome, given that P_{trpC}*::hph* inserts 1,401 bp. A hygromycin-resistant progeny from a sexual cross,
267 xKL9AR-17, was characterized by PCR analysis as harboring both the ΔLGIIK9het25 allele (Figure
268 S5B) and a wild type *mus-52*$^{+}$ allele. The final strain, NKL2 (genotype: *mat A*; Δ*LGIIK9het25::hph*),
269 had no noticeable growth defect from a WT strain (Figure S5C-D).

270 We performed chromatin-specific Hi-C [24], using either *Dpn*II to monitor gene-rich chromatin
271 contacts or *Mse*I to capture the interactions of AT-rich, gene-poor constitutive heterochromatin. Our
272 ΔLGIIK9het25 Hi-C replicates (four *Dpn*II and two *Mse*I replicates) show highly reproducible and
273 correlated interactions (Figure S6), allowing us to merge replicates into enzyme-specific datasets,
274 with the NKL2 *Dpn*II dataset containing 20.6M valid reads and the NKL2 *Mse*I dataset comprising
275 12.2M valid reads. All Hi-C datasets display the inter-chromosomal centromeric interactions that
276 occur independently from telomere clusters, indicating capture of biologically relevant structures
277 (Figures S7-S8); these chromosomal features were originally detailed in microscopic observations
278 of fluorescently labeled centromeric and telomeric proteins [25, 37]. As before, we selected similar
279 valid read numbers from previously published WT *Dpn*II and *Mse*I datasets for comparisons [24].

280 Compared to a WT *Dpn*II Hi-C dataset (Figure 2A), the deleted LGIIK9het25 region appears as a
281 large white "cross" devoid of Hi-C interactions on LGII in the NKL2 *Dpn*II contact probability matrix
282 (Figure 2B). Looking specifically at a 500 kb region surrounding LGIIK9het25, the WT dataset has
283 extensive intra-heterochromatic interactions within LGIIK9het25, and less prominent, but present,
284 heterochromatin-euchromatin contacts (Figure 2A). In contrast, the NKL2 has contact probability

285 loss, as few interactions occur in the raw interaction heatmap and sparse contacts at the diagonal in
286 the KR corrected dataset (Figure 2B), which, like the ΔK27 datasets (Figure S4), is due to a few reads
287 in both the ΔLGIIK9het25 *Dpn*II and MseI datasets mapping to repetitive DNA sequences present in
288 LGIIK9het25, within the nc14 reference genome, increasing contact probability bias (Figure S9). The
289 Hi-C contacts surrounding ΔLGIIK9het25 in NKL2 appear enhanced, as the flanking euchromatin
290 moderately gains contacts in the NKL2 *Dpn*II dataset, relative to a WT dataset (Figure 2A-B). Similar
291 contact probability changes occur in WT and NKL2 *Mse*I datasets, where in the WT dataset the
292 LGIIK9het25 region extensively contacts internal heterochromatin yet is isolated from surrounding
293 euchromatin, but the NKL2 dataset loses intra-LGIIK9het25 heterochromatic contacts yet gains
294 flanking euchromatin interactions (Figure 2C-D). Direct comparison of the WT and NKL2 *Dpn*II and
295 *Mse*I datasets surrounding LGIIK9het25 shows the contact probability gain between flanking
296 euchromatic regions when this separating heterochromatic region is deleted (Figure 2E-F,
297 arrowheads). The surrounding euchromatin may gain local, on-diagonal interactions, as shown in
298 the *Mse*I comparison (Figure 2F), possibly due to either reduced heterochromatic interactions or a
299 local contact capture bias in the NKL2 dataset. Between LG I and LG II, the LGIIK9het25 deletion
300 causes a loss of inter-heterochromatic region contacts, including from the largest non-centromeric
301 heterochromatic region on LG I (Figure 2G, white arrowhead), while the LG II centromere loses
302 inter-centromeric contacts but modestly gains interactions with interspersed heterochromatic
303 regions (Figure 2G, black arrowhead). Similar gains in inter-heterochromatic region interactions are
304 evident across the genome in the NKL2 *Mse*I Hi-C dataset, when compared to the WT *Mse*I dataset
305 (Figure S10), implying a dramatic shift in the heterochromatin bundle with LGIIK9het25 deletion.
306 When comparing the NKL2 *Dpn*II contact matrix to that of a WT strain, the inter-chromosomal
307 contact strength between centromere-proximal euchromatin and more-distant euchromatin on
308 chromosome arms is increased, yet chromosome-internal euchromatic contacts are reduced (Figure

309 S11), consistent with altered bundling between centromeres and interspersed heterochromatic
310 regions. Similarly, both ΔLGIIK9het25 Hi-C datasets have depleted inter-centromeric contacts; KR
311 correction reduces *Dpn*II contact biases (Figures S10-S11). While it is possible that the LGIIK9het25
312 deletion causes significant genome organization changes, these results may also highlight moderate
313 levels of variability in the Hi-C data derived from the population of nuclei in the NKL2 strain source
314 tissue. Here, valid genome organization differences would be amplified by subtle disparities in Hi-C
315 experiments. These biases occurred despite our use of the same *in situ* Hi-C protocol to generate
316 highly correlated NKL2 replicates (Figure S6), and how we performed the *Dpn*II NKL2 and *Mse*I WT
317 Hi-C experiments at the same time, which hypothetically would minimize experimental bias.
318 To assess changes between the WT and NKL2 strains independent of Hi-C restriction enzymes
319 and to compare datasets generated at the same time, we summed the *Dpn*II and *Mse*I datasets from
320 each strain and compared the summed contact probability matrices. The WT and NKL2 summed
321 datasets are similar, with more complete coverage in heterochromatic regions (Figure 12A-B), yet
322 moderately distant contacts in the NKL2 dataset are reduced. Direct comparison of the summed
323 matrices showed the NKL2 dataset with more local contacts and reduction of more distant
324 interactions, with the loss of contacts within the LGIIK9het25 region readily apparent (Figure S12C).
325 Thus, even when some Hi-C experiments performed at the same time are assessed, variation in
326 contact probability, hypothetically due to differences in genome organization that are enhanced in
327 individual Hi-C experiments, is evident. All told, the LGIIK9het25 deletion may affect the
328 organization of the entire Neurospora genome.
329
330 ***The LGIIK9het25 deletion still allows H3K9me3 deposition at nearby AT-rich loci but alters TAD-***
331 ***like structures.***
332 Upon deleting LGIIK9het25, the possibility exists that genome function, specifically H3K9me3

333 deposition on nearby AT-rich loci, is impacted. To assess if LGIIK9het25 loss prevents histone PTM
334 enrichment on surrounding heterochromatic regions, we performed H3K9me3-specific Chromatin
335 Immunoprecipitation-sequencing (ChIP-seq) on the NKL2 strain. The two NKL2 H3K9me3 ChIP-seq
336 replicates are highly reproducible (Figure S13) for merging into a single file that was normalized by
337 Reads Per Kilobase per Million (RPKM) for direct comparison to previously published WT H3K9me3
338 ChIP-seq datasets, although using spike-in DNA controls in ChIP-seq experiments performed at the
339 same time may be the best practice for assessing strain differences or relative enrichment levels [65,
340 66]. We mapped the ChIP-seq reads to either the nc14 WT genome or a "NKL2 genome", a reference
341 genome in which the P_{trpC}*::hph* sequence replaces the AT-rich DNA of LGIIK9het25; enhanced images
342 show low levels of background signal across the P_{trpC}*::hph* sequence in an NKL2 H3K9me3 ChIP-seq
343 dataset that are absent in WT H3K9me3 data (Figure S5E).

344 LG II exhibits an identical pattern of absolute H3K9me3 ChIP-seq enrichment across the AT-rich
345 regions surrounding LGIIK9het25, independent of the reference genome used for mapping reads.
346 For ChIP-seq data mapped to the WT nc14 genome, equal H3K9me3-enriched regions are observed,
347 except peaks to the right of LGIIK9het25 are shifted by ~110kb from the deletion site (Figure 3A),
348 given that genomic elements positions within our bigwig enrichment count files are shifted based
349 on input bam files having altered read mapping positions across this region. Qualitatively, the NKL2
350 H3K9me3 peaks may be higher (Figure 3A), possibly reflecting increased H3K9me3 purification
351 from the remaining constitutive heterochromatic regions or enhanced sequencing depth limiting
352 background signal, although we cannot make strict conclusions about relative H3K9me3
353 enrichment from experiments not performed at the same time. When H3K9me3 ChIP-seq data from
354 both strains was mapped to the NKL2 reference genome, the loss of LGIIK9het25 signal from the
355 WT dataset is apparent, while the remaining constitutive heterochromatic regions have identical LG
356 II genomic positions and absolute enrichment (Figure 3B).

357 To further assess local chromatin changes resulting from the LGIIK9het25 deletion, we examined
358 TAD-like loop structures on LG IIR. We chose parameters in TAD prediction that mostly placed TAD
359 borders for heterochromatic regions within H3K9me3-enriched domains to increase our chances of
360 predicting biologically relevant TADs, although TAD structure prediction within the same dataset
361 can vary [67]. We started by predicting TAD-like structures in WT and NKL2 *Dpn*II and *Mse*I datasets
362 mapped to the NKL2 reference genome to examine strain-specific changes in chromatin folding
363 without the LGIIK9het25 deletion signal gap. Clear TAD-like structure changes are observed at the
364 deletion site, with the euchromatin in the NKL2 ΔLGIIK9het25 *Dpn*II dataset having larger TAD-like
365 structures, while the NKL2 *Mse*I dataset has smaller on-diagonal TAD-like structures (Figures 4A-B,
366 black arrowheads); this difference likely stems from the chromatin monitored – and the density of
367 restriction sites, with AT-rich heterochromatin having more *Mse*I sites – in each Hi-C experiment.
368 The flanking TAD-like structures are nearly identical in both datasets, except for two larger TADs-
369 like structures in the NKL2 *Mse*I data (Figure 4A-B, open arrowheads). The use of Topdom [43] as
370 second TAD prediction program also showed TAD changes in the NKL2 *Dpn*II Hi-C data relative to
371 WT (Figure S14A), although the TAD changes differ from those predicted by hicExplorer[42]; the
372 Topdom TADs are highly similar in both WT and NKL2 *Mse*I Hi-C datasets (Figure S14B), highlighting
373 the challenges of fungal TAD prediction. Similar TAD-like structure changes across euchromatin are
374 observed in WT and NKL2 *Dpn*II datasets mapped to the nc14 (WT) genome, with larger TAD-like
375 structures predicted with the ΔLGIIK9het25 allele, as opposed to the smaller TAD-like structures in
376 WT datasets (Figure S14C). Interestingly, at the P_{trpC}*::hph* insertion, two novel yet small TAD-like
377 structures are observed in both NKL2 datasets, combined with additional stronger Hi-C interactions
378 in *Mse*I data (Figure 4A, purple line), and comparing the NKL2 contact probability and TADs to those
379 in the WT data highlighted the contact probability increase that alters chromatin folding in NKL2
380 (Figure 4B). These data suggest the constitutive P_{trpC} promoter could influence the local contacts

381 and expression of genes in this region. Finally, when TADs are predicted in contact probability
382 heatmaps independent of restriction enzyme used (e.g., in summed *Dpn*II and *Mse*I contact
383 probability matrices, mapped to either the nc14 or NKL2 reference genomes), subtle TAD changes
384 are seen across the ΔLGK9het25 deletion site despite good agreement between heterochromatin-
385 euchromatin boundaries and TAD borders (Figures 4C and S14D). Overall, it appears the
386 LGIIK9het25 deletion alters the local chromatin folding surrounding the deletion site.
387
388 ***The LGIIK9het25 deletion alters the three-dimensional folding of Neurospora chromosomes.***
389 It remains possible that this large constitutive heterochromatic region deletion alters
390 chromosome folding. To assess the 3D folding of LG II, we computationally predicted the LG II 3D
391 structure using WT and NKL2 ΔLGIIK9het25 Hi-C datasets. We chose to merge all *Dpn*II and *Mse*I
392 data together from each strain to maximize the possible Hi-C contacts across their genomes; we did
393 not combine *Dpn*II and *Mse*I data at ratios equivalent to the Neurospora chromatin distribution, as
394 previously performed [24]. With these summed contact probability matrices, we generated LG II 3D
395 structures using 3DMax [44] customized for biologically relevant structures in fungal genomes;
396 multiple structure prediction iterations occur prior to producing the final 3D structure.
397 In the WT strain, LG II has an elongated structure with condensed chromosome arms, a more
398 isolated centromere, telomeres localized to a single "side", and extensive intervening chromatin
399 loops (Figure 5A). Similar 3D structure prediction changes are observed on the other six WT
400 chromosomes (Figure S14). The LGIIK9het25 region forms a loop and associates with nearby
401 chromatin loops (Figure 5A), consistent with nine, moderately sized heterochromatic regions
402 present in the terminal 800 kb of the LG II right arm (Figure 3A). In contrast, the chromosome arms
403 within the LG II 3D structure of the NKL2 LGIIK9het25 deletion are more compact and wider, despite
404 similar centromere isolation, telomere locations, and looping of intervening chromatin (Figure 5B).

405 However, the terminal right arm of the output 3D structure for NKL2 LG II does not form any loops,
406 which suggests that our requirement for maintaining telomere clusters in fungal 3D structure
407 prediction influences how this NKL2 chromosome folds (Figure 5B). Similar folding differences
408 occur on each LG in NKL2, with some chromosomes, particularly LG I and LG IV - having drastically
409 altered 3D structures relative to WT (Figures S14, S15). Together, the LGIIK9het25 deletion modifies
410 the predicted 3D structures of Neurospora LGs.
411
412 ***The LGIIK9het25 deletion alters gene expression, which is correlated to differences in 3D***
413 ***genome folding.***
414 To understand if the removal of LGIIK9het25 could influence genome function by altering gene
415 expression, we assessed changes in polyadenylation messenger RNA sequencing (polyA mRNA-seq)
416 in WT and NKL2 strains. As a control for complete loss of constitutive heterochromatin function, we
417 examined gene expression changes in a Δ*dim-5* strain devoid of H3K9me3 genome-wide [30].
418 Volcano plots displaying the significant gene expression changes ($\log_2 > 3.0$ or < -3.0; adjusted p-
419 value < 0.001) in the NKL2 strain relative to the WT strain show 84 genes become significantly
420 upregulated and no genes significantly downregulated, (Figure 6A, left; Supplementary File S1);
421 additional differentially expressed genes (DEGs) could be indicated with less stringent cutoff values.
422 In contrast, the Δ*dim-5* strain has 175 DEGs compared to WT, and many genes have either increased
423 or decreased transcription (Figure 6A, right; Supplementary File S2), including the strong reduction
424 of the gene NCU04402 encoding DIM-5 (Figure 6B), confirming the Δ*dim-5* strain genotype. Many
425 Δ*dim-5* DEGs are found within altered H3K27me2/3 peaks (Figure S16) to possibly explain these
426 transcriptional changes, as facultative heterochromatin relocates to constitutive heterochromatic
427 regions in a Δ*dim-5* strain [51, 52]. The ΔLGIIK9het25 and Δ*dim-5* datasets each have unique DEGs,
428 as only 25 DEGs overlap both datasets. Notably, ΔLGIIK9het25 causes less drastic expression

429 changes relative to the Δ*dim-5* polyA mRNA-seq (Figure 6A-B). Further, no DEGs in the
430 ΔLGIIK9het25 dataset regulate chromatin or transcription (Supplementary File S3), although many
431 DEGs are hypothetical genes without defined functions, preventing a complete tally of the putative
432 regulatory genes. Interestingly, gene expression changes in the ΔLGIIK9het25 strain occur on each
433 chromosome (Figures 6B, S17), with many genes near H3K9me3-marked heterochromatic regions.
434 To assess if linear chromosome distance between DEGs and heterochromatic regions affects gene
435 expression, we measured the closest distance between each DEG transcription start site (TSS) and
436 the nearest heterochromatic region border, plotting the distance in groups (from 1-1,000 bp; 1,001-
437 10,000 bp; 10,001-100,000 bp; and 100,001-1 million [M] bp apart). Most DEGs (n = 51) are 10,001-
438 100,000 bp distant from the nearest H3K9me3-enriched border, with the second most DEGs (n =
439 23) found up to 1M bp distant (Figure S18), suggesting linear genomic distance has a minor
440 regulatory role. The single gene within 1,000 bp of a heterochromatic region, NCU08696, is directly
441 adjacent to LGIIK9het25 and is downregulated in the Δ*dim-5* strain but upregulated in
442 ΔLGIIK9het25 (Figure 6B, zoomed region), the latter possibly due to its proximity to the strong P_{trpC}
443 promoter. While longer chromosomes would be expected to have more DEGs, the short ~4.3 Mb LG
444 VII has more genes with changed expression (n = 24 DEGs) than either the ~10 Mb LG I (n = 20
445 DEGs) or the 6.0 Mb LG IV (n =11 DEGs) (Figures 6B and S16, Supplementary File S2). We conclude
446 that a single constitutive heterochromatic region impacts gene expression across the fungal genome.
447 To assess if altered 3D chromosome folding could explain the transcriptional changes in the
448 ΔLGIIK9het25 strain, we colored bins harboring DEGs on NKL2 chromosome models. Qualitatively,
449 the positions of the bins containing DEGs are modified on ΔLGIIK9het25 chromosome structures
450 relative to the WT chromosomes (Figures 6C-D, S19, S20). Specifically, on LG II, the bins with DEGs
451 appear more "enclosed" within the WT structure, while these same bins are repositioned to another
452 "face" of the NKL2 LG II structure (Figure 6C-D). Similar qualitative bin movements altering DEG

453 positions are observed on other LGs (Figures S19, S20).

454 Finally, we examined the positions of ΔLGIIK9het25 DEGs relative to the 3D folding predicted for
455 the entire WT and NKL2 genomes. Our 3D genome models maintain the biologically relevant [25,
456 37] single centromere cluster which is distinct from telomere bundles (Figure S21). The WT genome
457 model forms an elongated structure with the LGIIK9het25 region close to the structure top (Figure
458 7A), consistent with the "stretched" conformation of individual chromosomes (Figures 5, S18-S19)
459 and a previous report [68], despite different programs predicting each 3D structure. The NKL2
460 genome deleted of LGIIK9het25 is wider and less elongated (Figure 7B), similar to the individual
461 NKL2 chromosomes. Intriguingly, the 20 kb bins with ΔLGIIK9het25 DEGs are qualitatively oriented
462 towards the WT genome periphery, while the same bins are more centrally localized in the NKL2
463 genome, consistent with a hypothesis where enhanced transcription machinery access increases
464 gene expression. We conclude that the deletion of a single heterochromatic region alters the 3D
465 genome conformation and disrupts normal genome function in the Neurospora nucleus.

466

467 **Discussion**

468 Here, we examined if facultative and constitutive heterochromatic regions organize the fungal
469 genome by performing Hi-C on strains harboring silent region deletions. Our results suggest that
470 gene-rich facultative heterochromatic loci are plastic in nature, as a facultative heterochromatin
471 deletion simply fuses nearby H3K27me2/3-enriched regions within the linear chromosome, which
472 minimally impacts facultative heterochromatin clusters. Specifically, the subtelomere bundling at
473 the terminal ~150 kb of each LG is maintained in the ΔK27 strain. Subtelomere clustering may be
474 compromised by larger deletions or deletions that target the terminal ~150 kb of chromosome ends.
475 Consistent with these hypotheses, genome-wide loss of H3K27me2/3 in a Neurospora Δ*set-7* (Δ*kmt-*
476 *6*) strain can release subtelomere clusters from the nuclear periphery [37], suggesting at least some

477 subtelomeric H3K27me2/3 is needed for telomeres to associate with the nuclear membrane. It is
478 possible that larger or more telomere-proximal deletions would disrupt subtelomere clustering, but
479 further facultative heterochromatin deletions have not been attempted [34]. Still, it is likely that
480 Neurospora tolerates alterations to gene-rich genomic loci, assuming no essential genes are deleted,
481 given the absence of wide-ranging topological or physiological consequences. Since most genes
482 enriched with H3K27me2/3 are novel genes with hypothetical functions [33], perhaps Neurospora
483 tolerates subtelomeric structural variants if facultative heterochromatin is present. In contrast,
484 some Fusarium species require H3K27me2/3 for normal growth [69], meaning structural variants
485 in facultative heterochromatic regions may be lethal in other fungi.

486 We also assessed the role of a constitutive heterochromatic region for organizing the Neurospora
487 genome. The most recent Neurospora reference genome (nc14) [24] has ~200 interspersed
488 H3K9me3-enriched regions distributed over seven chromosomes, and apart from the centromeres
489 and telomeres on each LG necessary for chromosome function, the remaining interspersed
490 heterochromatic regions have been dismissed as "junk DNA". However, when we delete the largest,
491 non-centromeric heterochromatic region on LG II, genome organization and function are impacted
492 without a severe phenotypic effect. Specifically, the heterochromatic regions still present in NKL2
493 uniquely cluster when LGIIK9het25 is deleted, as we observe gains in intra- and inter-chromosomal
494 heterochromatin contacts, including between interspersed heterochromatic regions and
495 centromeres. Any altered inter-heterochromatic region bundling may reflect valid genome
496 organization changes in NKL2 nuclei, as hypothetically, the LGIIK9het25 deletion would cause the
497 remaining interspersed heterochromatic regions to form novel and variable inter-heterochromatin
498 contacts in each nucleus. These organizational changes may then be amplified by the Hi-C protocol,
499 resulting in the increased contact probability variation we observe. Therefore, a limitation of this
500 study is that we cannot differentiate between these two sources of variability. Still, since genome

501 organization can vary between individual cells across a population [70], it is likely that LGIIK9het25
502 removal causes contact probability matrix variation from altered heterochromatin bundling. Future
503 controlled fungal Hi-C experiments coupled with computational modeling are warranted to assess
504 the day-to-day Hi-C experiment variability to shed light on valid genome organization changes in
505 WT and ΔLGIIK9het25 strains. Nevertheless, LGIIK9het25 appears to primarily have a structural
506 role in anchoring silent regions on Neurospora chromosomes, while other heterochromatic regions
507 may impact genome function to a greater extent. Additional H3K9me3-enriched region deletions, or
508 progressive truncations of LGIIK9het25, could have elucidated other effects on heterochromatin
509 bundling or fungal genome function. Further, it is possible that additional WT or NKL2 genome
510 organization or function effects could have been discovered with different growth conditions, such
511 as alternative carbon or nitrogen sources, osmolarities, or temperatures, in a manner synonymous
512 to the jet-like chromatin structures across secondary metabolite clusters observed when *Fusarium*
513 *graminearum* is cultured in excess nitrogen [71].

514 Our ΔLGIIK9het25 data favor a model where the Neurospora heterochromatin bundle is
515 dynamic, but we cannot exclude the possibility that proteins binding to specific DNA motifs in AT-
516 rich DNA promote heterochromatin aggregation. We suggest that any dynamic heterochromatin
517 clustering could be mediated by Liquid Liquid Phase Separation or a chromatin binding protein,
518 such as Heterochromatin Protein-1 (HP1) [72–74]. Since HP1 loss does not radically disrupt the
519 Neurospora heterochromatin bundle [25], multiple factors, acting redundantly, could drive fungal
520 heterochromatin aggregation. Consistent with this hypothesis, HP1-independent pericentromere
521 clusters are observed in Drosophila [75]. It is currently unknown how eukaryotic constitutive
522 heterochromatic regions bundle, although histone post-translational modifications and/or DNA
523 methylation contribute to fungal genome organization. Specifically in Neurospora, subtelomeric
524 H3K27me2/3 loss causes genome disorder and reduced telomere tethering, while deletion of the

525 HCHC histone deacetylase complex causes constitutive heterochromatin hyperacetylation to
526 increase inter-heterochromatic region contacts; heterochromatin hyperacetylation coupled with
527 $5^{m}C$ loss, reduces heterochromatin compartmentalization [37, 47]. Future experiments should
528 elucidate other chromatin-specific mechanisms for organizing eukaryotic genomes.

529 The LGIIK9het25 deletion also changes local chromatin structure and 3D genome folding. In a
530 manner synonymous to the ΔK27 strain, the LGIIK9het25 deletion fuses flanking chromatin
531 segments, as shown by contact gains between neighboring euchromatin bins. However, this deletion
532 of LGIIK9het25 alters the predicted TADs, and therefore the regional chromatin looping, across the
533 fused chromatin in two TAD prediction programs. Since interspersed heterochromatic regions in
534 filamentous fungi anchor the bases of TAD-like structures [9, 24–26, 36], in a mechanism
535 tantamount to CTCF forming metazoan loops [10], removing a heterochromatic region could allow
536 interactions between distant euchromatic regions. However, the extensive inter-TAD interactions in
537 fungi [24–26] complicate TAD prediction, and non-uniform TAD-like structures in Neurospora could
538 minimize the functional consequences of altered chromatin loops. While we used TAD prediction
539 parameters to keep heterochromatic region TADs in domains of H3K9me3 to accurately report
540 biologically relevant TADs, one limitation of our study is that euchromatic TAD/loop prediction is
541 particularly challenging in Neurospora. In fact, variable intra- and inter-heterochromatin bundling
542 across chromosomes could cause variability in euchromatin loops in nuclei populations, similar to
543 the variable TAD boundaries reported in different human cell types [76]. Still, our study has
544 functional implications for higher eukaryotic systems. While fungi and metazoans employ some
545 unique chromatin folding mechanisms, the deletion of a metazoan constitutive heterochromatic
546 region could also disrupt TADs to promote new contacts across the normally isolated TAD-internal
547 chromatin, in a manner synonymous to our results in fungi. Thus, loss of a H3K9me3-enriched
548 region from a metazoan genome could alter TAD compartmentalization or misregulate gene

549 expression if several smaller TADs are merged into a larger TAD. Unfortunately, the consequences to
550 metazoan genome function would be more dire, given how TAD boundary dysfunction compromises
551 proper gene expression [6–8]. In fact, our chromosome and genome structure predictions suggest
552 local looping changes could manifest into a unique folding pattern for the entire genome. Here, the
553 ΔLGIIK9het25 deletion caused each chromosome, and the genome, to qualitatively form
554 conformations distinct from the WT genome. While these models are merely predictions and should
555 be interpreted lightly, it is impactful that the repositioning of a single locus has the potential to alter
556 the 3D structure of a whole genome. Hypothetically, despite the species-specific differences in TADs
557 or loops, syntenic changes of linear chromosomal DNA could disorganize a species' genome, causing
558 functional changes.

559 Our results also suggest a single constitutive heterochromatic region impacts the transcription
560 of distant genes in the WT Neurospora genome. The gene expression changes we observe in the
561 LGIIK9het25 deletion differ from those in a Δ*dim-5* strain if all H3K9me3 is removed, the latter strain
562 causing numerous genes both strongly up- and down-regulated [37], suggesting LGIIK9het25 has a
563 minor but real impact on genome function. Overall, this single constitutive heterochromatic region
564 may subtly repress Neurospora gene expression. Control of gene expression by H3K9me3-enriched
565 regions in Neurospora was hypothesized from observations of strong contacts between genes and
566 constitutive heterochromatic regions in high-resolution Hi-C datasets [24]. However, it is difficult to
567 imagine that a single LGIIK9het25 region deletion directly causes gene expression changes genome
568 wide. More likely, the ΔLGIIK9het25 allele alters the positioning of the heterochromatin bundle –
569 and the nearby euchromatin – at the nuclear periphery, which repositions some gene promoters for
570 increased transcription machinery accessibility. This hypothesis is supported by modeling the gene
571 expression changes on the ΔLGIIK9het25 chromosomes and across the genome and reasonably
572 explains gene activation in the NKL2 strain. Of course, altered promoters can also drive gene

573 expression changes, as observed by the strong P_{trpC} promoter in the NKL2 deletion strain increasing
574 transcription of gene NCU08696 immediately adjacent to LGIIK9het25, although the possibility
575 exists that these changes are a consequence of the loss of AT-rich DNA. In contrast, NCU08696, and
576 other genes near constitutive heterochromatic regions, are downregulated in the Δ*dim-5* strain
577 lacking H3K9me3, suggesting that some H3K9me3-enriched regions directly control transcription.
578 Similarly, the proper expression of the Neurospora *met-8* gene requires the immediately adjacent
579 interspersed constitutive heterochromatic region [77]. Together, our results show gene regulation
580 across the fungal genome – even genes on different chromosomes – may depend on a single
581 constitutive heterochromatic region. In metazoans, H3K9me3 enrichment at a gene promoter can
582 repress expression, as the control of mouse embryonic stem cell identity requires the co-deposition
583 of H3K9me3 and H3K36me3 for transcriptional repression [78]. Thus, in addition to the canonical
584 repression of transposable elements and repetitive sequences in eukaryotic genomes [79–82],
585 H3K9me3 can directly regulate transcription. We propose that heterochromatin-mediated gene
586 regulation also occurs through 3D organization, where genes interact with H3K9me3-enriched
587 regions. In this model, genes would associate with constitutive heterochromatic regions at the more
588 repressive periphery for reducing transcription; should these genes be reoriented to the active
589 nuclear center, transcription would increase. It is feasible that constitutive heterochromatic regions
590 could indirectly regulate more "evolutionarily new" or fungal specific genes, in a similar manner as
591 facultative heterochromatin in Neurospora [33], and examining all genes regulated by constitutive
592 heterochromatin in RNA-seq datasets from multiple region deletion strains could assess the
593 evolutionary age of genes controlled by H3K9me3-marked regions. Currently, it is unknown how
594 constitutive heterochromatic regions may regulate gene expression, but an attractive model
595 includes HP1 binding to small amounts of H3K9me3 deposited at gene promoters to allow
596 aggregation with the constitutive heterochromatin bundle; the amount of H3K9me3 needed to

implement this regulation is unknown, but could be minor or occur only in a sub-population of nuclei, given the near background levels of H3K9me3 across Neurospora genic regions in ChIP-seq of mycelial populations. Still, fungi may be more apt to employ this hypothetical mechanism to regulate transcription, as opposed to metazoans, given the more-promiscuous contacts across fungal TAD-like structures and the extensive inter-chromosomal contacts in a Rabl chromosome conformation [9, 24–26, 36]. Recently, the histone methyltransferase SETDB1, which catalyzes H3K9me3 in metazoans, was shown to maintain gene expression and drive chromatin compartmentalization [83]. Thus, constitutive heterochromatic regions have additional, underappreciated roles in both genome organization and function across diverse species.

Conclusions

Our work here has directly assessed how one large H3K9me3-marked silent genomic region impacts fungal genome organization and function. Here, the deletion of a 110.6kb H3K9me3-enriched region alters the hierarchical 3D genome organization in *Neurospora crassa*, with chromatin fibers, TAD-like structures, individual chromosomes, and the fungal genome all having altered conformations. The H3K9me3 deposition on neighboring gene poor regions still occurs despite this 110.6 kb constitutive heterochromatic region deletion, yet this deletion increases gene expression genome wide, which 3D genome modeling suggests is due to upregulated genes being mispositioned into the transcriptionally active nucleus center. Since the Neurospora genome contains 200+ other H3K9me3-regions, it is likely that each silent region similarly contributes to genome function. Since many eukaryotic genomes have H3K9me3-enriched constitutive heterochromatic regions, including many metazoans, the aggregation of constitutive heterochromatin may be a conserved mechanism for organizing eukaryotic genomes and that individual H3K9me3-enriched regions may regulate eukaryotic transcription. Further research in multiple species should help elucidate novel functional

621 roles for this pervasive yet evolutionarily conserved "junk DNA" retained in eukaryotic genomes.

622

623 **Declarations**

624 *Ethics approval and consent to participate*

625 Not applicable

626

627 *Consent for publication*

628 Not applicable

629

630 *Availability of Data and Materials*

631 All genomic datasets are deposited in the NCBI GEO under the SuperSeries accession number
632 GSE269235. Individual datasets have the subseries numbers GSE269228 (ChIP-seq), GSE269229
633 (Hi-C), and GSE269230 (polyA mRNA-seq). All Neurospora strains are available upon request.

634

635 *Competing interests*

636 The authors declare that they have no competing interests.

637

638 *Funding*

639 Funding was provided by a UCCS Undergraduate Research Academy award to A.T.R., start-up
640 funds from the UCCS College of Engineering and Applied Science to O.O., a Maximizing Investigators
641 Research Award grant (1R35GM150402-01) to O.O., start-up funds from the UCCS College of Letters,
642 Arts, and Sciences to A.D.K., and a NIH Academic Research Enhancement Award grant
643 (1R15GM140396-01) to A.D.K.

644

645 *Authors' contributions*

646 A.T.R. and A.D.K. designed research; A.T.R., A.P., J.V., C.G.C, O.O. and A.D.K. performed research;
647 A.T.R., A.P., J.V., C.G.C., O.O. and A.D.K. analyzed data; and A.T.R., A.P., J.V., C.G.C., O.O. and A.D.K. wrote
648 the paper.

649

650 *Acknowledgements*

651 The authors thank Sara Rodriguez, Yulia Shtanko, and Ashley Scadden for Hi-C library generation
652 help; Sara Hanson (Colorado College) for TapeStation use and RNA-seq protocol advice; the
653 University of Oregon GC3F for Illumina library sequencing service, and Klocko lab members and
654 UCCS Department of Chemistry & Biochemistry colleagues for helpful comments and discussions.

655

656 **References**

657 1. Cremer T, Cremer C. Chromosome territories, nuclear architecture and gene regulation in
658 mammalian cells. Nat Rev Genet. 2001;2:292–301.

659 2. Misteli T. Beyond the Sequence: Cellular Organization of Genome Function. Cell. 2007;128:787–
660 800.

661 3. Dekker J. Gene Regulation in the Third Dimension. Science. 2008;319:1793–4.

662 4. Sexton T, Cavalli G. The Role of Chromosome Domains in Shaping the Functional Genome. Cell.
663 2015;160:1049–59.

664 5. Bonev B, Cavalli G. Organization and function of the 3D genome. Nat Rev Genet. 2016;17:661–78.

665 6. Flavahan WA, Drier Y, Liau BB, Gillespie SM, Venteicher AS, Stemmer-Rachamimov AO, et al.
666 Insulator dysfunction and oncogene activation in IDH mutant gliomas. Nature. 2016;529:110–4.

667 7. Dixon JR, Xu J, Dileep V, Zhan Y, Song F, Le VT, et al. Integrative detection and analysis of structural
668 variation in cancer genomes. Nat Genet. 2018;50:1388–98.

669 8. Northcott PA, Lee C, Zichner T, Stütz AM, Erkek S, Kawauchi D, et al. Enhancer hijacking activates
670 GFI1 family oncogenes in medulloblastoma. Nature. 2014;511:428–34.

671 9. Torres DE, Reckard AT, Klocko AD, Seidl MF. Nuclear genome organization in fungi: From gene
672 folding to Rabl chromosomes. FEMS Microbiol Rev. 2023;47(3):fuad021.

673 10. Rao SSP, Huntley MH, Durand NC, Stamenova EK, Bochkov ID, Robinson JT, et al. A 3D Map of
674 the Human Genome at Kilobase Resolution Reveals Principles of Chromatin Looping. Cell.
675 2014;159:1665–80.

676 11. Lieberman-Aiden E, Berkum NL van, Williams L, Imakaev M, Ragoczy T, Telling A, et al.
677 Comprehensive Mapping of Long-Range Interactions Reveals Folding Principles of the Human
678 Genome. Science. 2009;326:289–93.

679 12. Luger K, Mäder AW, Richmond RK, Sargent DF, Richmond TJ. Crystal structure of the nucleosome
680 core particle at 2.8 Å resolution. Nature. 1997;389:251–60.

681 13. Luger K, Richmond TJ. DNA binding within the nucleosome core. Curr Opin Struc Biol.
682 1998;8:33–40.

683 14. Rao SSP, Huang S-C, Hilaire BGS, Engreitz JM, Perez EM, Kieffer-Kwon K-R, et al. Cohesin Loss
684 Eliminates All Loop Domains. Cell. 2017;171:305-320.e24.

685 15. Mizuguchi T, Fudenberg G, Mehta S, Belton J-M, Taneja N, Folco HD, et al. Cohesin-dependent
686 globules and heterochromatin shape 3D genome architecture in *S. pombe*. Nature. 2014;516:432–5.

687 16. Campos EI, Reinberg D. Histones: Annotating Chromatin. Annu Rev Genet. 2009;43:559–99.

688 17. Dixon JR, Selvaraj S, Yue F, Kim A, Li Y, Shen Y, et al. Topological Domains in Mammalian Genomes
689 Identified by Analysis of Chromatin Interactions. Nature. 2012;485:376–80.

690 18. Kind J, Pagie L, de Vries SS, Nahidiazar L, Dey SS, Bienko M, et al. Genome-wide Maps of Nuclear
691 Lamina Interactions in Single Human Cells. Cell. 2015;163:134–47.

692 19. Falk M, Feodorova Y, Naumova N, Imakaev M, Lajoie BR, Leonhardt H, et al. Heterochromatin
693 drives compartmentalization of inverted and conventional nuclei. Nature. 2019;570:395–9.

694 20. Schoenfelder S, Sexton T, Chakalova L, Cope NF, Horton A, Andrews S, et al. Preferential
695 associations between co-regulated genes reveal a transcriptional interactome in erythroid cells. Nat
696 Genet. 2010;42:53–61.

697 21. Mahajan A, Yan W, Zidovska A, Saintillan D, Shelley MJ. Euchromatin Activity Enhances
698 Segregation and Compaction of Heterochromatin in the Cell Nucleus. Phys Rev X. 2022;12:041033.

699 22. Hoencamp C, Dudchenko O, Elbatsh AMO, Brahmachari S, Raaijmakers JA, Schaik T van, et al. 3D
700 genomics across the tree of life reveals condensin II as a determinant of architecture type. Science.
701 2021;372:984–9.

702 23. Imakaev M, Fudenberg G, McCord RP, Naumova N, Goloborodko A, Lajoie BR, et al. Iterative
703 correction of Hi-C data reveals hallmarks of chromosome organization. Nat Methods. 2012;9:999–
704 1003.

705 24. Rodriguez S, Ward A, Reckard AT, Shtanko Y, Hull-Crew C, Klocko AD. The genome organization
706 of *Neurospora crassa* at high resolution uncovers principles of fungal chromosome topology. G3
707 Genes Genomes Genetics. 2022;12(5):jkac053.

708 25. Galazka JM, Klocko AD, Uesaka M, Honda S, Selker EU, Freitag M. Neurospora chromosomes are
709 organized by blocks of importin alpha-dependent heterochromatin that are largely independent of
710 H3K9me3. Genome Res. 2016;26:1069–80.

711 26. Torres DE, Kramer HM, Tracanna V, Fiorin GL, Cook DE, Seidl MF, et al. Implications of the three-
712 dimensional chromatin organization for genome evolution in a fungal plant pathogen. Nat Commun.
713 2023;15:1701.

714 27. Galagan JE, Calvo SE, Borkovich KA, Selker EU, Read ND, Jaffe D, et al. The genome sequence of
715 the filamentous fungus *Neurospora crassa*. Nature. 2003;422:859–68.

716 28. Lewis ZA, Honda S, Khlafallah TK, Jeffress JK, Freitag M, Mohn F, et al. Relics of repeat-induced
717 point mutation direct heterochromatin formation in *Neurospora crassa*. Genome Res. 2009;19:427–
718 37.

719 29. Nurk S, Koren S, Rhie A, Rautiainen M, Bzikadze AV, Mikheenko A, et al. The complete sequence
720 of a human genome. Science. 2022;376:44–53.

721 30. Tamaru H, Zhang X, McMillen D, Singh PB, Nakayama J, Grewal SI, et al. Trimethylated lysine 9
722 of histone H3 is a mark for DNA methylation in *Neurospora crassa*. Nat Genet. 2003;34:75–9.

723 31. Lewis ZA, Adhvaryu KK, Honda S, Shiver AL, Knip M, Sack R, et al. DNA Methylation and Normal
724 Chromosome Behavior in Neurospora Depend on Five Components of a Histone Methyltransferase
725 Complex, DCDC. PLoS Genet. 2010;6:e1001196.

726 32. Klocko AD, Uesaka M, Ormsby T, Rountree MR, Wiles ET, Adhvaryu KK, et al. Nucleosome
727 Positioning by an Evolutionarily Conserved Chromatin Remodeler Prevents Aberrant DNA
728 Methylation in Neurospora. Genetics. 2019;211:563–78.

729 33. Jamieson K, Rountree MR, Lewis ZA, Stajich JE, Selker EU. Regional control of histone H3 lysine
730 27 methylation in Neurospora. Proc Natl Acad Sci. 2013;110:6027–32.

731 34. Jamieson K, McNaught KJ, Ormsby T, Leggett NA, Honda S, Selker EU. Telomere repeats induce
732 domains of H3K27 methylation in Neurospora. Elife. 2018;7:e31216.

733 35. Wiles ET, Selker EU. H3K27 methylation: a promiscuous repressive chromatin mark. Curr Opin
734 Genet Dev. 2017;43:31–7.

735 36. Winter DJ, Ganley ARD, Young CA, Liachko I, Schardl CL, Dupont P-Y, et al. Repeat elements
736 organise 3D genome structure and mediate transcription in the filamentous fungus *Epichloë*
737 *festucae*. PLoS Genet. 2018;14:e1007467.

738 37. Klocko AD, Ormsby T, Galazka JM, Leggett NA, Uesaka M, Honda S, et al. Normal chromosome
739 conformation depends on subtelomeric facultative heterochromatin in *Neurospora crassa*. Proc Natl
740 Acad Sci. 2016;113:15048–53.

741 38. Davis RH. Neurospora: contributions of a model organism. Oxford University Press; 2000.

742 39. Honda S, Selker EU. Tools for Fungal Proteomics: Multifunctional Neurospora Vectors for Gene
743 Replacement, Protein Expression and Protein Purification. Genetics. 2009;182:11–23.

744 40. Miao VPW, Freitag M, Selker EU. Short TpA-rich segments of the ζ-η region induce DNA
745 methylation in *Neurospora crassa*. J Mol Biol. 2000;300:249–73.

746 41. Langmead B, Salzberg SL. Fast gapped-read alignment with Bowtie 2. Nat Methods. 2012;9:357–
747 9.

748 42. Ramírez F, Bhardwaj V, Arrigoni L, Lam KC, Grüning BA, Villaveces J, et al. High-resolution TADs
749 reveal DNA sequences underlying genome organization in flies. Nat Commun. 2018;9:189.

750 43. Shin H, Shi Y, Dai C, Tjong H, Gong K, Alber F, et al. TopDom: an efficient and deterministic
751 method for identifying topological domains in genomes. Nucleic Acids Res. 2016;44:e70–e70.

752 44. Oluwadare O, Zhang Y, Cheng J. A maximum likelihood algorithm for reconstructing 3D
753 structures of human chromosomes from chromosomal contact data. BMC Genom. 2018;19:161.

754 45. Trieu T, Cheng J. 3D genome structure modeling by Lorentzian objective function. Nucleic Acids
755 Res. 2017;45:1049–58.

756 46. Pettersen EF, Goddard TD, Huang CC, Meng EC, Couch GS, Croll TI, et al. UCSF ChimeraX:
757 Structure visualization for researchers, educators, and developers. Protein Sci. 2021;30:70–82.

758 47. Scadden AW, Graybill AS, Hull-Crew C, Lundberg TJ, Lande NM, Klocko AD. Histone deacetylation
759 and cytosine methylation compartmentalize heterochromatic regions in the genome organization
760 of *Neurospora crassa*. Proc Natl Acad Sci. 2023;120:e2311249120.

761 48. Li H, Handsaker B, Wysoker A, Fennell T, Ruan J, Homer N, et al. The Sequence Alignment/Map
762 format and SAMtools. Bioinformatics. 2009;25:2078–9.

763 49. Ramírez F, Ryan DP, Grüning B, Bhardwaj V, Kilpert F, Richter AS, et al. deepTools2: a next
764 generation web server for deep-sequencing data analysis. Nucleic Acids Res. 2016;44:W160-5.

765 50. Robinson JT, Thorvaldsdóttir H, Winckler W, Guttman M, Lander ES, Getz G, et al. Integrative
766 genomics viewer. Nat Biotechnol. 2011;29:24–6.

767 51. Jamieson K, Wiles ET, McNaught KJ, Sidoli S, Leggett N, Shao Y, et al. Loss of HP1 causes depletion
768 of H3K27me3 from facultative heterochromatin and gain of H3K27me2 at constitutive
769 heterochromatin. Genome Res. 2016;26:97–107.

770 52. Basenko EY, Sasaki T, Ji L, Prybol CJ, Burckhardt RM, Schmitz RJ, et al. Genome-wide
771 redistribution of H3K27me3 is linked to genotoxic stress and defective growth. Proc Natl Acad Sci.
772 2015;112:E6339–48.

773 53. Klocko AD, Summers CA, Glover ML, Parrish R, Storck WK, McNaught KJ, et al. Selection and
774 Characterization of Mutants Defective in DNA Methylation in *Neurospora crassa*. Genetics.
775 2020;216:genetics.303471.2020.

776 54. Kamei M, Ameri AJ, Ferraro AR, Bar-Peled Y, Zhao F, Ethridge CL, et al. IMITATION SWITCH is
777 required for normal chromatin structure and gene repression in PRC2 target domains. Proc Natl
778 Acad Sci. 2021;118:e2010003118.

779 55. Zhang Y, Park C, Bennett C, Thornton M, Kim D. Rapid and accurate alignment of nucleotide
780 conversion sequencing reads with HISAT-3N. Genome Res. 2020;31:1290–5.

781 56. Anders S, Pyl PT, Huber W. HTSeq--a Python framework to work with high-throughput
782 sequencing data. Bioinform Oxf Engl. 2015;31:166–9.

783 57. Love MI, Huber W, Anders S. Moderated estimation of fold change and dispersion for RNA-seq
784 data with DESeq2. Genome Biol. 2014;15:550.

785 58. Team Rs. RStudio: Integrated Development for R. Boston, MA: RStudio, PBC; 2020.

786 59. Team RC. R: A language and environment for statistical computing. Vienna, Austria: R
787 Foundation for Statistical Computing; 2021.

788 60. Knight PA, Ruiz D. A fast algorithm for matrix balancing. Ima J Numer Anal. 2013;33:1029–47.

789 61. Ninomiya Y, Suzuki K, Ishii C, Inoue H. Highly efficient gene replacements in Neurospora strains
790 deficient for nonhomologous end-joining. Proc Natl Acad Sci. 2004;101:12248–53.

791 62. Selker E. Premeiotic Instability Of Repeated Sequences In *Neurospora crassa*. Annu Rev Genet.
792 1990;24:579–613.

793 63. Gladyshev E, Kleckner N. Direct recognition of homology between double helices of DNA in
794 *Neurospora crassa*. Nat Commun. 2014;5:3509–3509.

795 64. Kück U, Hoff B. Application of the nourseothricin acetyltransferase gene (nat1) as dominant
796 marker for the transformation of filamentous fungi. Fungal Genet Rep. 2006;53:9–11.

797 65. Bonhoure N, Bounova G, Bernasconi D, Praz V, Lammers F, Canella D, et al. Quantifying ChIP-seq
798 data: a spiking method providing an internal reference for sample-to-sample normalization.
799 Genome Res. 2014;24:1157–68.

800 66. Orlando DA, Chen MW, Brown VE, Solanki S, Choi YJ, Olson ER, et al. Quantitative ChIP-Seq
801 Normalization Reveals Global Modulation of the Epigenome. Cell Reports. 2014;9:1163–70.

802 67. Zufferey M, Tavernari D, Oricchio E, Ciriello G. Comparison of computational methods for the
803 identification of topologically associating domains. Genome Biol. 2018;19:217.

804 68. Poinsignon T, Gallopin M, Grognet P, Malagnac F, Lelandais G, Poulain P. 3D models of fungal
805 chromosomes to enhance visual integration of omics data. NAR Genom Bioinform. 2023;5:lqad104.

806 69. Connolly LR, Smith KM, Freitag M. The *Fusarium graminearum* Histone H3 K27
807 Methyltransferase KMT6 Regulates Development and Expression of Secondary Metabolite Gene
808 Clusters. PLoS Genet. 2013;9:e1003916.

809 70. Nagano T, Lubling Y, Stevens TJ, Schoenfelder S, Yaffe E, Dean W, et al. Single-cell Hi-C reveals
810 cell-to-cell variability in chromosome structure. Nature. 2013;502:59–64.

811 71. Shao W, Wang J, Zhang Y, Zhang C, Chen J, Chen Y, et al. The jet-like chromatin structure defines
812 active secondary metabolism in fungi. Nucleic Acids Res. 2024;52:4906–21.

813 72. Larson AG, Elnatan D, Keenen MM, Trnka MJ, Johnston JB, Burlingame AL, et al. Liquid droplet
814 formation by HP1α suggests a role for phase separation in heterochromatin. Nature. 2017;547:236–
815 40.

816 73. Freitag M, Hickey PC, Khlafallah TK, Read ND, Selker EU. HP1 Is Essential for DNA Methylation
817 in Neurospora. Mol Cell. 2004;13:427–34.

818 74. Zenk F, Zhan Y, Kos P, Löser E, Atinbayeva N, Schächtle M, et al. HP1 drives *de novo* 3D genome
819 reorganization in early Drosophila embryos. Nature. 2021;593:289–93.

820 75. Stutzman AV, Hill CA, Armstrong RL, Gohil R, Duronio RJ, Dowen JM, et al. Heterochromatic 3D
821 genome organization is directed by HP1a- and H3K9-dependent and independent mechanisms. Mol
822 Cell. 2024;84(11):2017-35.e6.

823 76. Sauerwald N, Singhal A, Kingsford C. Analysis of the structural variability of topologically
824 associated domains as revealed by Hi-C. NAR Genom Bioinform. 2019;2:lqz008.

825 77. Yang S, Li W, Qi S, Gai K, Chen Y, Suo J, et al. The highly expressed methionine synthase gene of
826 *Neurospora crassa* is positively regulated by its proximal heterochromatic region. Nucleic Acids Res.
827 2014;42:6183–95.

828 78. Barral A, Pozo G, Ducrot L, Papadopoulos GL, Sauzet S, Oldfield AJ, et al. SETDB1/NSD-dependent
829 H3K9me3/H3K36me3 dual heterochromatin maintains gene expression profiles by bookmarking
830 poised enhancers. Mol Cell. 2022;82:816-832.e12.

831 79. Padeken J, Zeller P, Towbin B, Katic I, Kalck V, Methot SP, et al. Synergistic lethality between
832 BRCA1 and H3K9me2 loss reflects satellite derepression. Genes Dev. 2019;33:436–51.

833 80. Padeken J, Methot SP, Gasser SM. Establishment of H3K9-methylated heterochromatin and its
834 functions in tissue differentiation and maintenance. Nat Rev Mol Cell Biol. 2022;23:623–40.

835 81. Herberg S, Simeone A, Oikawa M, Jullien J, Bradshaw CR, Teperek M, et al. Histone H3 lysine 9
836 trimethylation is required for suppressing the expression of an embryonically activated
837 retrotransposon in *Xenopus laevis*. Sci Rep. 2015;5:14236.

838 82. Zhao S, Lu J, Pan B, Fan H, Byrum SD, Xu C, et al. TNRC18 engages H3K9me3 to mediate silencing
839 of endogenous retrotransposons. Nature. 2023;623:633–42.

840 83. Keenan CR, Coughlan HD, Iannarella N, Fierro AT del, Keniry A, Johanson TM, et al. Suv39h-
841 catalyzed H3K9me3 is critical for euchromatic genome organization and the maintenance of gene
842 transcription. Genome Res. 2024;34:556–71.

843

844 **Figure Legends**

845 **Figure 1. A strain harboring a 47.4 kilobase deletion of a H3K27me2/3-enriched domain has**
846 **minimal genome organization change.** (A-B) Contact probability heatmaps of *Dpn*II
847 (euchromatin-specific) *in situ* Hi-C datasets at 20 kb resolution across Linkage Group VI (LG VI) of
848 the (A) WT or (B) N4933 strains, the latter deleted of a 47.4kb H3K27me2/3-enriched region
849 ("ΔK27"). Enhanced heatmaps show the terminal 500 kb of LG VI, harboring ΔK27, at 5 kb
850 resolution. Each Hi-C image displays the raw contact probability heatmap above the diagonal and
851 the Knight Ruiz (KR) [60] corrected contact probability heatmap below the diagonal; KR correction
852 reduces inherent biases in contact probability matrices. Scalebars shown below the images. Images
853 of wild type H3K9me3 (green) and H3K27me2/3 (purple) ChIP-seq tracks, displayed on IGV [50],
854 above and to the right. The purple line in (A) shows the WT location of the H3K27me2/3-enriched
855 region deleted in the ΔK27 strain, while the black arrowhead in (B) shows the increased contact
856 probability of flanking euchromatin in ΔK27. (C) KR corrected contact probability heatmaps of the
857 *Dpn*II *in situ* Hi-C datasets of WT and ΔK27 strains primarily showing on-diagonal contacts at 5 kb
858 bin resolution. Wild type H3K9me3 ChIP-seq (green), H3K27me2/3 ChIP-seq (purple), and gene
859 (gray) tracks shown below. Scalebar to the left. The black arrowhead shows the increased contact
860 probability of euchromatin flanking the ΔK27 deletion, while the gray arrowhead shows the contact
861 probability loss at a putative transposable element (*sly-1*, gene NCU09969). (D-E) Contact

862 probability heatmaps of the WT and ΔK27 telomere interactions, with the (D) intra-chromosomal
863 (LG VI left and right telomeres) or inter-chromosomal (LG VI left telomere and LG V right telomere)
864 contacts shown. Telomere schematic (with the green circle showing the telomere repeat position),
865 and tracks of H3K27me2/3 ChIP-seq (purple) or genes (gray) shown above and right. The red "X"
866 covers the deleted H3K27me2/3 domain, while the black arrowhead shows the deletion site contact
867 depletion.
868
869 **Figure 2. A ~110 kb H3K9me3-enriched domain deletion alters constitutive heterochromatic**
870 **region clustering.** (A-D) Contact probability heatmaps, presented as in Figure 1, of (A-B) *Dpn*II
871 (euchromatin-specific) and (C-D) *Mse*I (heterochromatin specific) *in situ* Hi-C datasets at 20 kb
872 resolution across LG II of (A, C) WT or (B, D) NKL2 strains, the latter deleted of the 25th H3K9me3-
873 enriched region from the LG II left telomere ("ΔLGIIK9het25"). The purple line in A shows the
874 deleted LGIIK9het25 region. Enhanced (5 kb) resolution heatmaps show the 500 kb surrounding
875 the ΔLGIIK9het25 allele, as in Figure 1A-B. (E-F) Images showing the $\log_2$ change in Hi-C contact
876 probability between WT and ΔLGIIK9het25 strains in (E) *Dpn*II (euchromatin-specific) or (F) *Mse*I
877 (heterochromatin-specific) 5 kb resolution datasets over the 500 kb surrounding the ΔLGIIK9het25
878 allele. The scalebar of contact probability changes is shown below. (G) Images showing the change
879 in inter-chromosomal *Mse*I Hi-C contact probability between LG I and the (top) LG II centromere or
880 (bottom) LGIIK9het25 interspersed heterochromatic region.
881
882 **Figure 3. The LGIIK9het25 deletion does not compromise H3K9me3 deposition at other**
883 **constitutive heterochromatic regions in the NKL2 strain.** (A-B) Images of WT (dark green) or
884 NKL2 ΔLGIIK9het25 (light green) H3K9me3 ChIP-seq and gene (gray) tracks, displayed on IGV, of
885 the entire LG II chromosome or enhanced regions. H3K9me3 ChIP-seq reads were mapped to the

886 (A) WT nc14 or (B) NKL2 ΔLGIIK9het25 reference genomes. Numbers in the Figure 3A enhanced
887 panel count the heterochromatic regions from the LG II left telomere, while the black arrowheads
888 show the LGIIK9het25 DNA deletion. The purple line shows the ~110 kb of DNA missing from the
889 NKL2 genome (shifting all H3K9me3 peaks to the right of the deletion by ~110 kb). The red arrow
890 in B shows the position of the inserted P_{trpC}*::hph* gene in NKL2.
891
892 **Figure 4. The LGIIK9het25 deletion alters the predicted TAD-like structures in the**
893 **surrounding chromatin.** (A) Contact probability heatmaps of *Dpn*II (KR corrected) or *Mse*I (raw)
894 *in situ* Hi-C datasets of WT and ΔLGIIK9het25 strains primarily showing on-diagonal contacts at 5
895 kb bin resolution, mapped to the NKL2 ΔLGIIK9het25 reference genome. Wild type H3K9me3 ChIP-
896 seq (green) and gene (gray) tracks shown below. The contact probability scalebar is shown to the
897 left of each heatmap. Predicted TAD-like structures, as determined by hicFindTADs in hicExplorer,
898 are indicated by black triangles. Black arrowheads indicate altered TAD-like structures surrounding
899 the LGIIK9het25 deletion, while white arrowheads show changed TAD-like structures in flanking
900 euchromatin. The red arrow shows the position of the P_{trpC}*::hph* gene inserted within the NKL2
901 reference genome, while the purple line shows increased chromatin contacts at the P_{trpC} promoter.
902 (B) A heatmap of the changes in contact probability between *Mse*I Hi-C datasets of WT and
903 ΔLGIIK9het25 strains, displayed as in A. The TAD-like structures predicted in WT (black) or
904 ΔLGIIK9het25 (blue) strains by hicFindTADs in hicExplorer are shown (triangles). (C) Contact
905 probability heatmaps, presented as in A, of WT and ΔLGIIK9het25 strains in which *Dpn*II and *Mse*I
906 Hi-C dataset were summed prior to KR correction.
907
908 **Figure 5. The predicted 3D folding of a single chromosome is changed with the LGIIK9het25**
909 **deletion.** (A-B) Images depicting the predicted 3D structures of LG II from (A) WT or (B) NKL2

910 ΔLGIIK9het25 strains at 20 kb resolution. The green region highlights the LGIIK9het25 region in the
911 WT structure. The enhanced image shows the chromatin folding of the LG II right arm surrounding
912 the LGIIK9het25 region in a WT strain. The arrow shows the LGIIK9het25 deletion site.
913
914 **Figure 6. The LGIIK9het25 region deletion causes increased gene expression genome wide.**
915 (A) Volcano plots showing the $\log_2$ fold change from WT expression levels of all Neurospora genes
916 verses adjusted p-values from (left) the NKL2 ΔLGIIK9het25 or (right) the Δ*dim-5* strains. Red
917 points are genes with significant expression changes ($\log_2$ fold changes > 3.0 or < -3.0 and adjusted
918 p-values < 0.001). The number of differentially expressed genes (DEGs) is indicated at the top. (B)
919 Images of IGV tracks showing WT H3K9me3 ChIP-seq (green), genes (gray), or the "up" ($\log_2$ > 3.0;
920 red) or "down" ($\log_2$ < -3.0; blue) DEGs. The purple "X" symbols cover LGIIK9het25 deleted in the
921 NKL2 strain, while the black arrows show the positions of genes NCU08696 or *dim-5* (NCU04402).
922 (C-D) Images depicting the predicted 3D modeling of LG II from (C) WT or (D) NKL2 ΔLGIIK9het25
923 strains at 20 kb resolution. The green region highlights the LGIIK9het25 region in the WT structure,
924 while 20 kb bins containing DEGs in the NKL2 strain, relative to a WT strain are colored red; the
925 same bins are marked on both structures. The arrow in D shows the LGIIK9het25 deletion site.
926
927 **Figure 7. The predicted 3D genome structure and DEG positions are altered upon**
928 **LGIIK9het25 deletion.** (A-B) Images depicting the predicted 3D genome structure of (A) WT or (B)
929 NKL2 ΔLGIIK9het25 strains. The left image is the side view of the genome structure; the right image
930 is where the genome structure is rotated up 90°, showing the centromere cluster. The green region
931 highlights the LGIIK9het25 region in the WT structure, while the 20 kb bins containing DEGs in the
932 NKL2 ΔLGIIK9het25 strain are colored red.

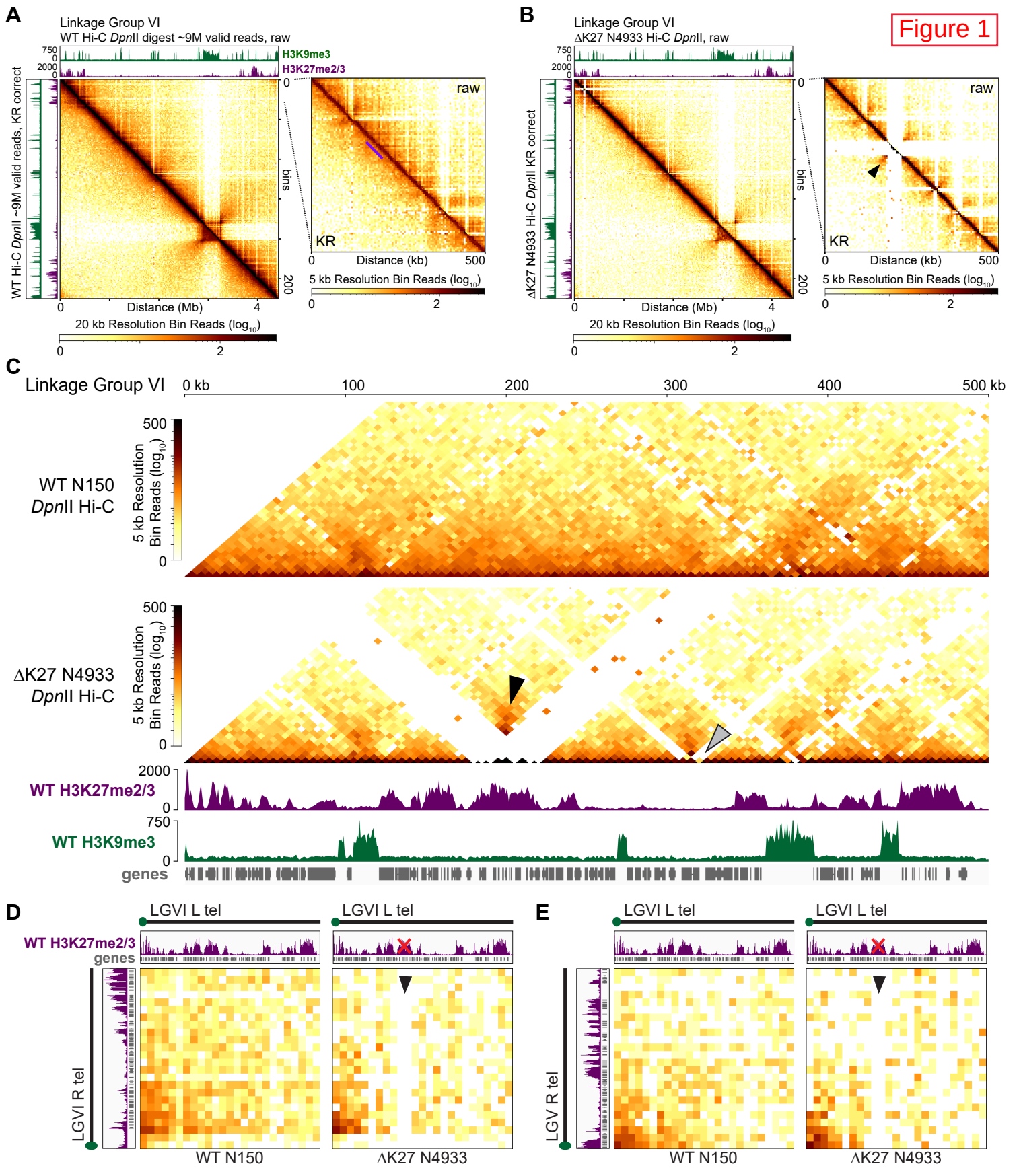
Figure 1
A
Linkage Group VI
WT Hi-C DpnII digest ~9M valid reads, raw
H3K9me3
H3K27me2/3
WT Hi-C DpnII ~9M valid reads, KR correct
raw
KR
bins
Distance (Mb)
Distance (kb)
20 kb Resolution Bin Reads (log10)
5 kb Resolution Bin Reads (log10)
B
Linkage Group VI
ΔK27 N4933 Hi-C DpnII, raw
ΔK27 N4933 Hi-C DpnII KR correct
C
Linkage Group VI
0 kb
100
200
300
400
500 kb
WT N150 DpnII Hi-C
ΔK27 N4933 DpnII Hi-C
5 kb Resolution Bin Reads (log10)
WT H3K27me2/3
WT H3K9me3
genes
D
E
LGVI L tel
LGVI R tel
LGV R tel
WT N150
ΔK27 N4933

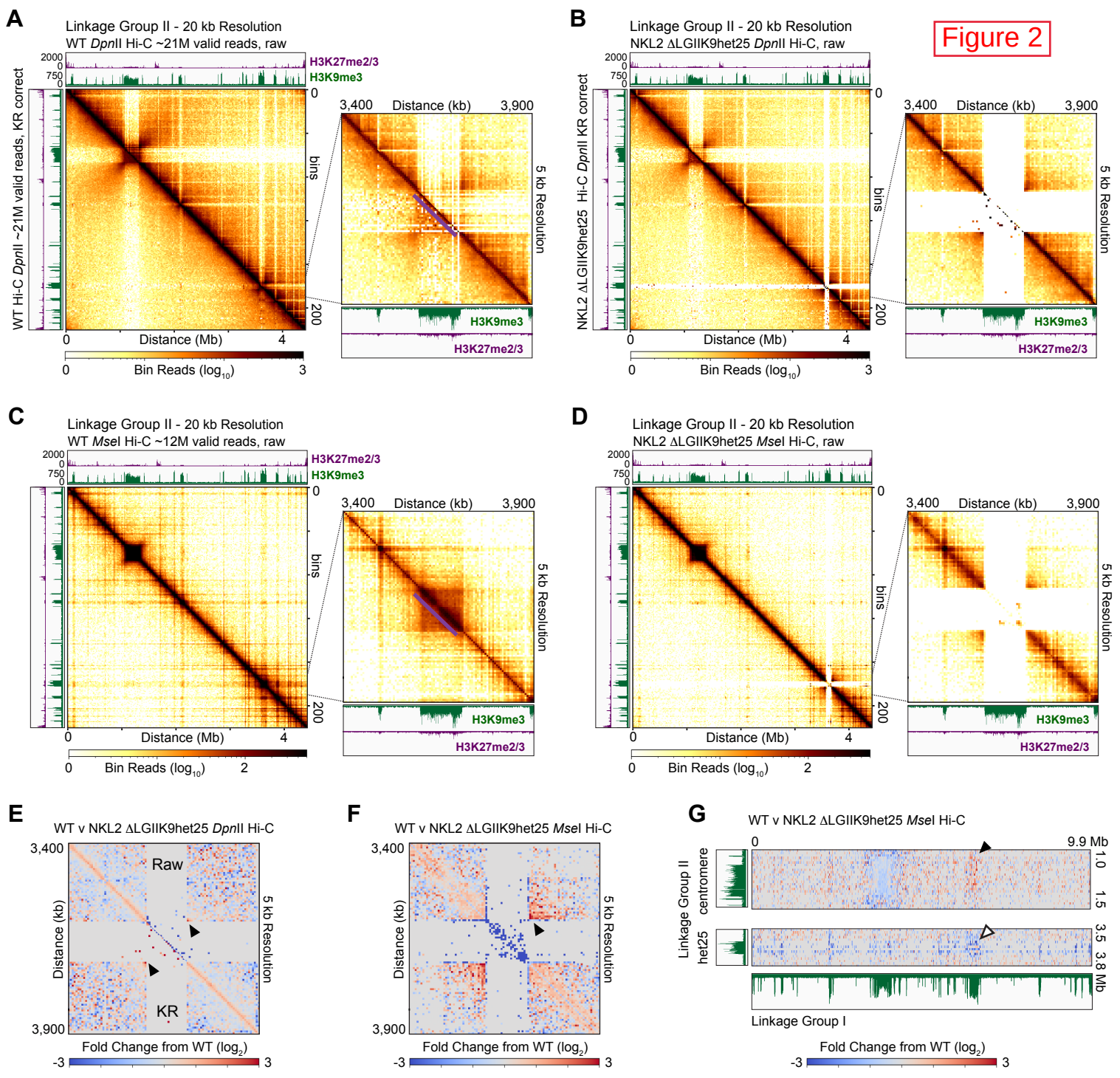
Figure 2
A
Linkage Group II - 20 kb Resolution
WT DpnII Hi-C ~21M valid reads, raw
H3K27me2/3
H3K9me3
WT Hi-C DpnII ~21M valid reads, KR correct
bins
Distance (Mb)
Bin Reads (log10)
3,400
Distance (kb)
3,900
5 kb Resolution
B
Linkage Group II - 20 kb Resolution
NKL2 ΔLGIIK9het25 DpnII Hi-C, raw
NKL2 ΔLGIIK9het25 Hi-C DpnII KR correct
C
Linkage Group II - 20 kb Resolution
WT MseI Hi-C ~12M valid reads, raw
D
Linkage Group II - 20 kb Resolution
NKL2 ΔLGIIK9het25 MseI Hi-C, raw
E
WT v NKL2 ΔLGIIK9het25 DpnII Hi-C
Raw
KR
Distance (kb)
Fold Change from WT (log2)
F
WT v NKL2 ΔLGIIK9het25 MseI Hi-C
G
WT v NKL2 ΔLGIIK9het25 MseI Hi-C
9.9 Mb
Linkage Group II
centromere
het25
Linkage Group I

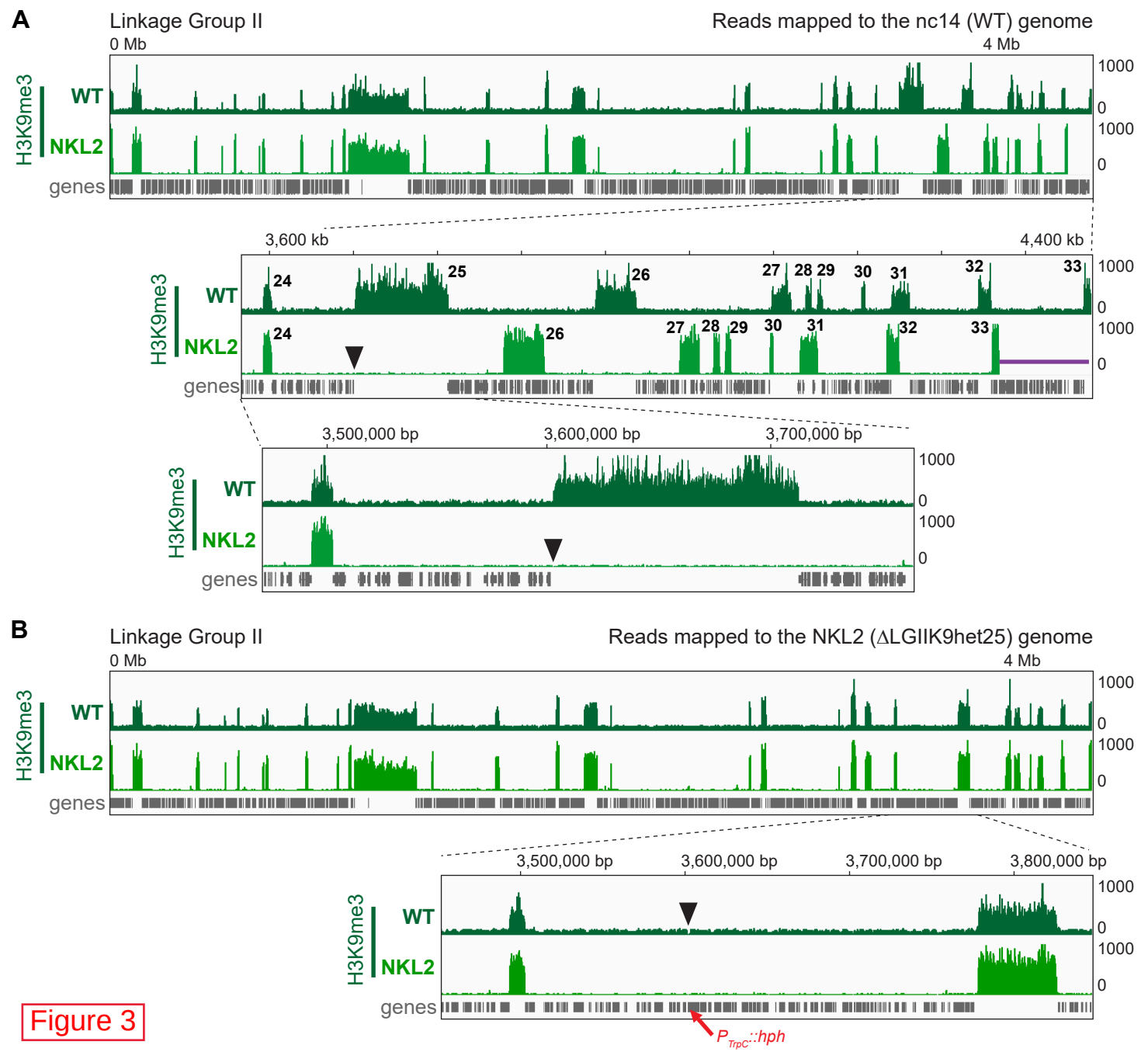
A
Linkage Group II
Reads mapped to the nc14 (WT) genome
0 Mb
4 Mb
H3K9me3
WT
NKL2
genes
1000
0
3,600 kb
4,400 kb
24
25
26
27
28
29
30
31
32
33
3,500,000 bp
3,600,000 bp
3,700,000 bp
B
Linkage Group II
Reads mapped to the NKL2 (ΔLGIIK9het25) genome
3,800,000 bp
P_{TrpC}::hph
Figure 3

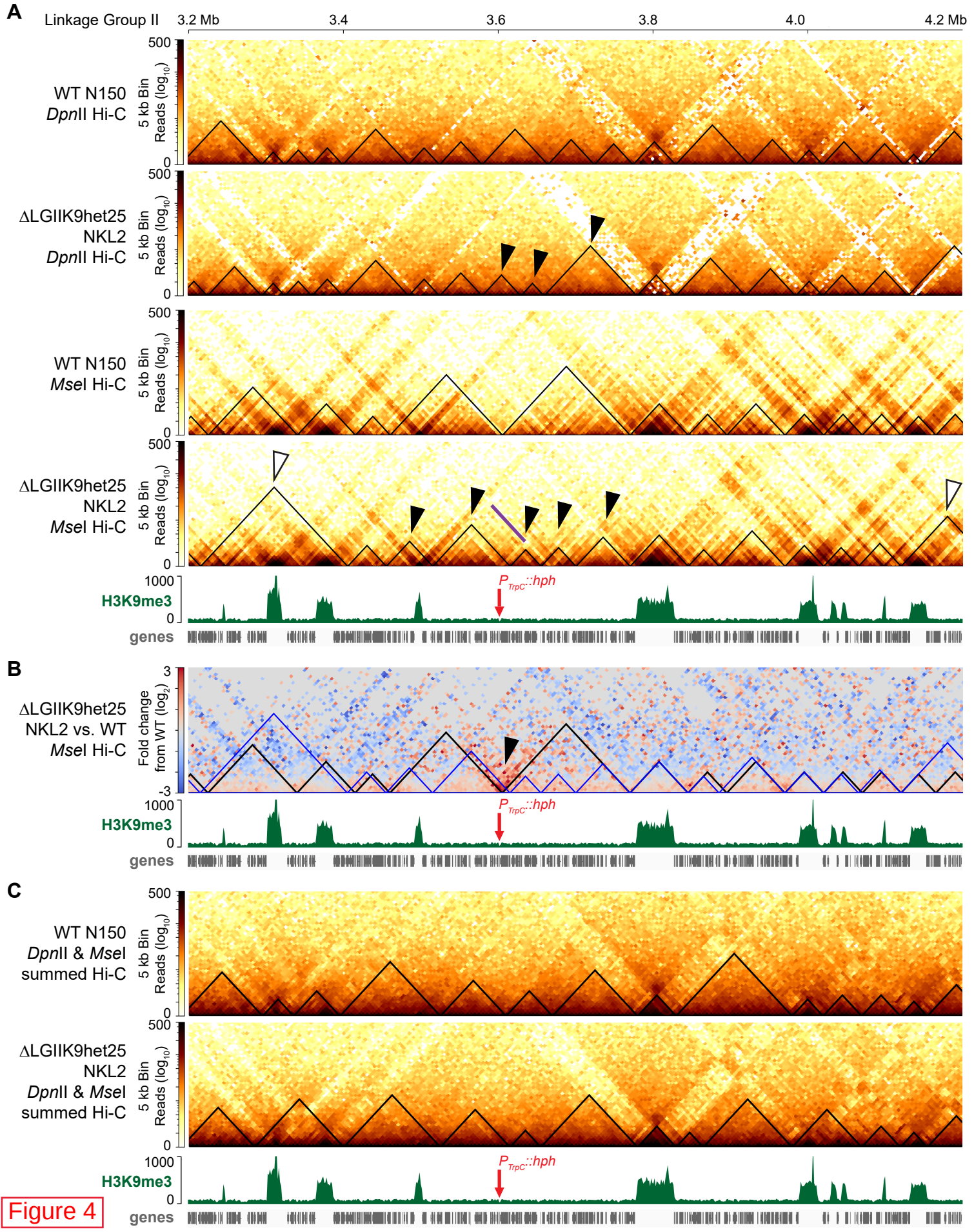
A
Linkage Group II
3.2 Mb
3.4
3.6
3.8
4.0
4.2 Mb
WT N150
DpnII Hi-C
ΔLGIIK9het25
NKL2
DpnII Hi-C
WT N150
MseI Hi-C
ΔLGIIK9het25
NKL2
MseI Hi-C
5 kb Bin
Reads (log10)
500
0
1000
H3K9me3
genes
PTrpC::hph
B
ΔLGIIK9het25
NKL2 vs. WT
MseI Hi-C
Fold change
from WT (log2)
3
-3
C
WT N150
DpnII & MseI
summed Hi-C
ΔLGIIK9het25
NKL2
DpnII & MseI
summed Hi-C

Figure 4

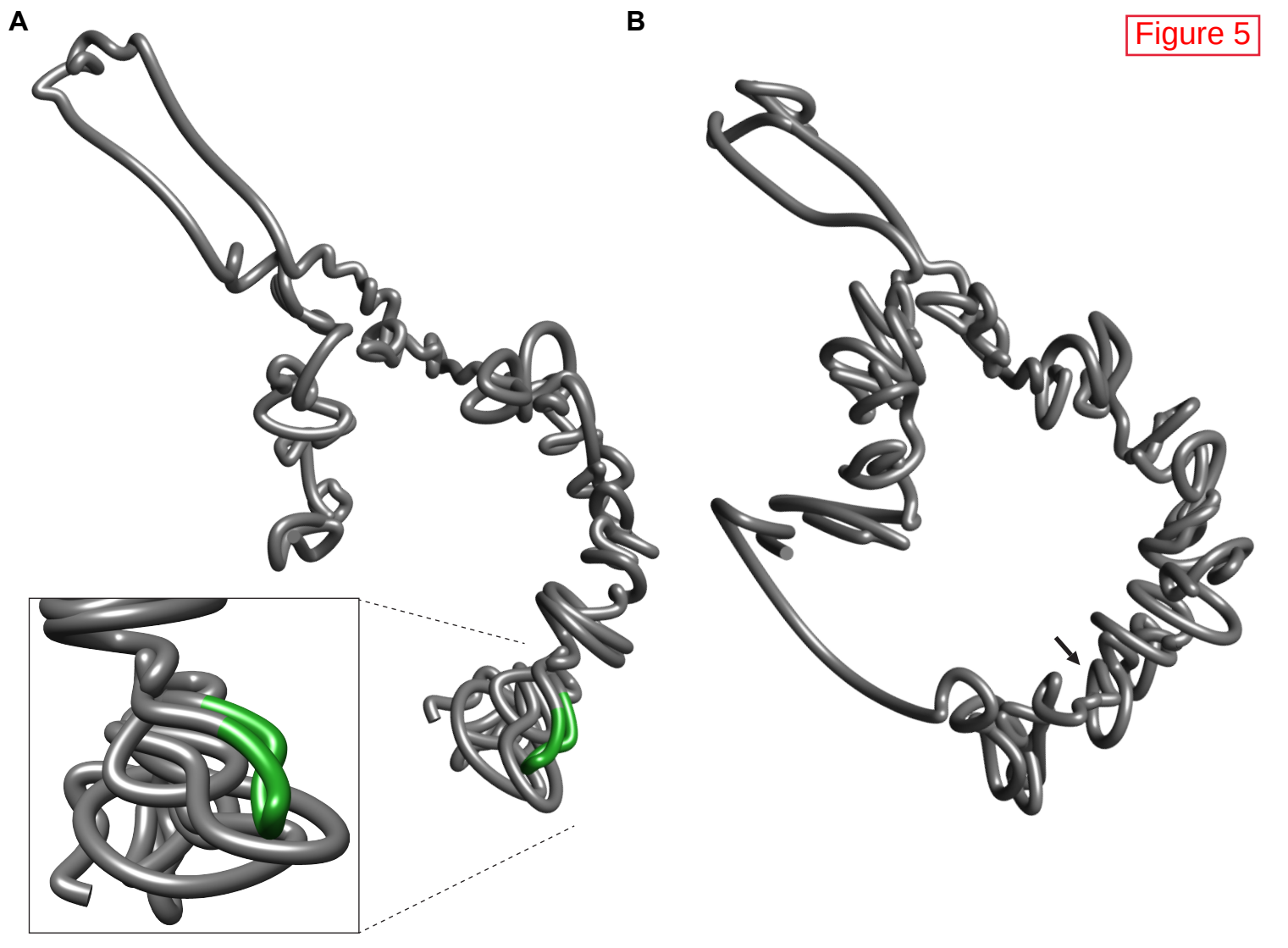
A
B
Figure 5

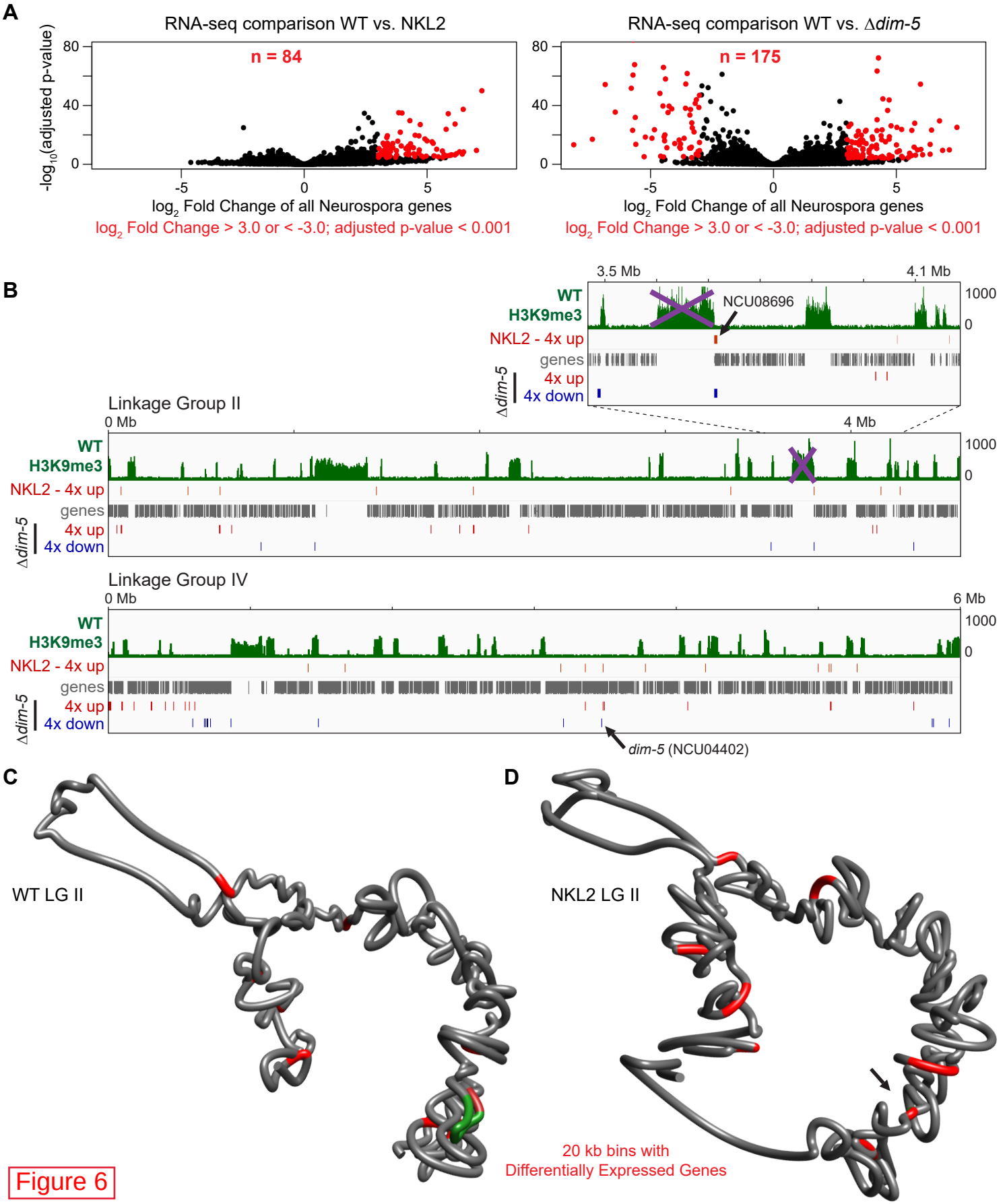
A
RNA-seq comparison WT vs. NKL2
n = 84
-log10(adjusted p-value)
log2 Fold Change of all Neurospora genes
log2 Fold Change > 3.0 or < -3.0; adjusted p-value < 0.001
RNA-seq comparison WT vs. Δdim-5
n = 175
log2 Fold Change of all Neurospora genes
log2 Fold Change > 3.0 or < -3.0; adjusted p-value < 0.001
B
3.5 Mb
4.1 Mb
WT
H3K9me3
NCU08696
NKL2 - 4x up
genes
Δdim-5
4x up
4x down
Linkage Group II
0 Mb
4 Mb
Linkage Group IV
6 Mb
dim-5 (NCU04402)
C
WT LG II
D
NKL2 LG II
20 kb bins with
Differentially Expressed Genes

Figure 6

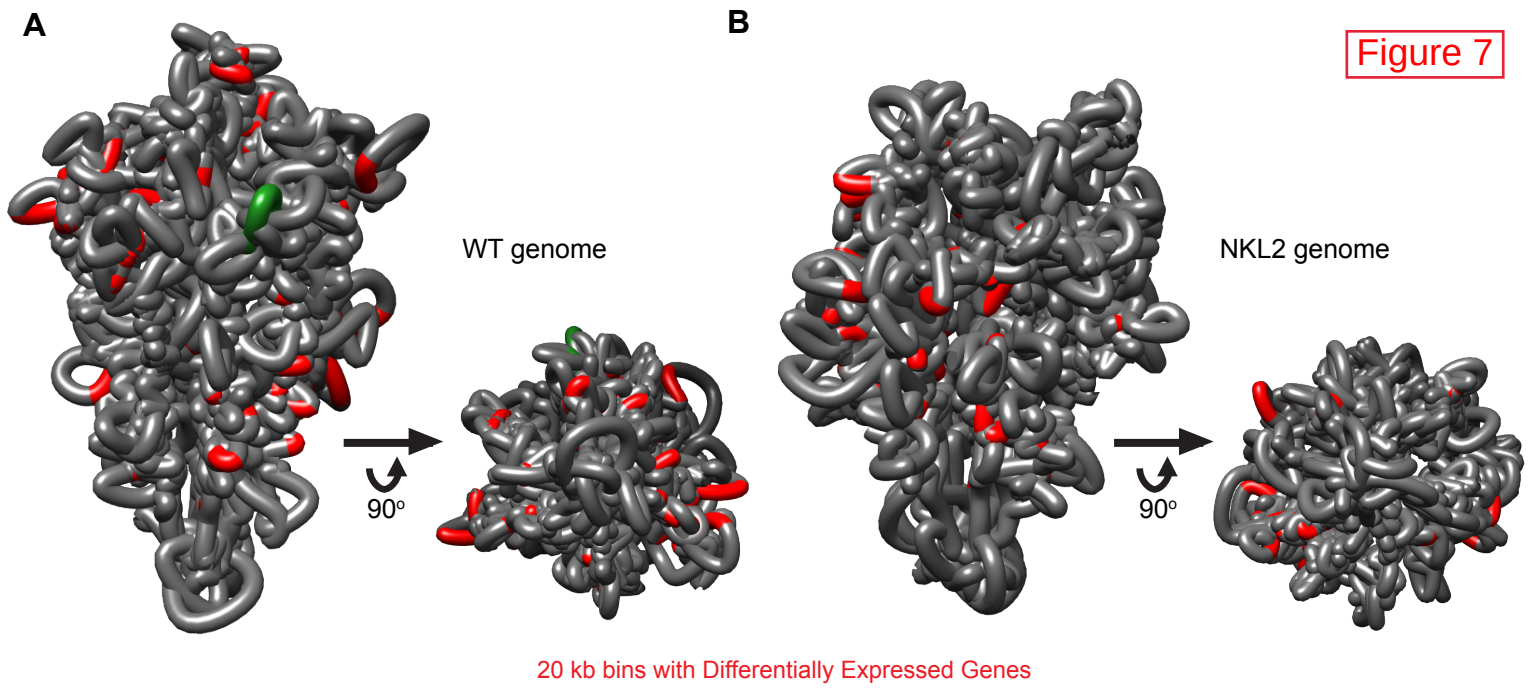
A
B
Figure 7
WT genome
NKL2 genome
90°
90°
20 kb bins with Differentially Expressed Genes